THE JOURNAL OF BIOLOGICAL CHEMISTRY VOL. 291, NO. 1, pp. 11–27, January 1, 2016

Structural Basis of Ribosomal S6 Kinase 1 (RSK1) Inhibition by S100B Protein

MODULATION OF THE EXTRACELLULAR SIGNAL-REGULATED KINASE (ERK) SIGNALING CASCADE IN A CALCIUM-DEPENDENT WAY[*] [◆]

Received for publication, August 18, 2015, and in revised form, October 30, 2015 Published, JBC Papers in Press, November 2, 2015, DOI 10.1074/jbc.M115.684928

Gergő Gógl[‡], Anita Alexa[§], Bence Kiss[‡], Gergely Katona[¶], Mihály Kovács[‖], Andrea Bodor[**], Attila Reményi[§1], and László Nyitray[‡2]

From the [‡]Department of Biochemistry, [‖]ELTE-MTA "Momentum" Motor Enzymology Research Group, Department of Biochemistry, and [**]Institute of Chemistry Eötvös Loránd University, 1117 Budapest, Hungary, the [§]"Momentum" Protein Interaction Group, Institute of Enzymology, Research Center for Natural Sciences, Hungarian Academy of Sciences, 1117 Budapest, Hungary, and the [¶]Department of Chemistry and Molecular Biology, University of Gothenburg, 40530 Gothenburg, Sweden

Mitogen-activated protein kinases (MAPK) promote MAPK-activated protein kinase activation. In the MAPK pathway responsible for cell growth, ERK2 initiates the first phosphorylation event on RSK1, which is inhibited by Ca^{2+}-binding S100 proteins in malignant melanomas. Here, we present a detailed *in vitro* biochemical and structural characterization of the S100B-RSK1 interaction. The Ca^{2+}-dependent binding of S100B to the calcium/calmodulin-dependent protein kinase (CaMK)-type domain of RSK1 is reminiscent of the better known binding of calmodulin to CaMKII. Although S100B-RSK1 and the calmodulin-CAMKII system are clearly distinct functionally, they demonstrate how unrelated intracellular Ca^{2+}-binding proteins could influence the activity of the CaMK domain-containing protein kinases. Our crystallographic, small angle x-ray scattering, and NMR analysis revealed that S100B forms a "fuzzy" complex with RSK1 peptide ligands. Based on fast-kinetics experiments, we conclude that the binding involves both conformation selection and induced fit steps. Knowledge of the structural basis of this interaction could facilitate therapeutic targeting of melanomas.

The vertebrate-specific S100 proteins belong to the EF-hand-containing, Ca^{2+}-binding superfamily of proteins with more than 20 paralogs in the human proteome (1, 2). They are small (~100 amino acids) and mostly homodimeric proteins where each monomer can bind two calcium ions. In their Ca^{2+}-bound form, each monomer exposes a hydrophobic surface and becomes capable of binding to target proteins. In most cases, two partner proteins bind to one S100 dimer symmetrically; however, there are a few examples where an elongated motif interacts with the two identical hydrophobic grooves simultaneously and asymmetrically (3, 4). S100 proteins can be found both intra- and extracellularly. On the cell surface, they can bind to receptors (such as receptor for advanced glycosylation end product) and activate ERK/p38 mitogen-activated protein kinase (MAPK) pathways indirectly (5, 6). Despite the fact that these small proteins have been extensively studied for decades, the precise and specific intracellular role of most S100 proteins still remains to be determined.

It has recently been shown that S100B can form a complex with ribosomal S6 kinase 1 (RSK1) in malignant melanoma cell lines, and this interaction negatively affects phosphorylation of the C-terminal Ca^{2+}/calmodulin-dependent kinase (CaMK)[3]-type domain of RSK1 by ERK1/2 (7). In malignant melanomas, S100B expression is highly elevated, which can be used as a prognostic marker for the disease (8). Moreover, S100B is being explored as a therapeutic target for treating melanomas by inhibiting its protein-protein interactions (9).

RSK1 belongs to the group of MAPK-activated protein kinases (MAPKAPK) (10). MAPKAPKs are downstream cytoplasmic targets of ERK and/or p38 MAPKs and belong to the CaMK-type protein kinase superfamily (11). Inactive MAPKAPKs are in an autoinhibited form where the C-terminal inhibitory helix (αL) blocks substrate as well as ATP binding. This inhibitory helix is followed by a short linker and an MAPK-binding linear motif, where the latter determines MAPK binding specificity (12, 13). The first step of MAPKAPK activation is activation loop (AL) phosphorylation by its cognate MAPK. Next, the autoinhibitory helix is extruded by the phosphorylated AL via an

[*] This work was supported in part by Hungarian National Research Fund (OTKA) Grants K108437 (to L. N.) and NK101072 (to A. B.), the Momentum Program of the Hungarian Academy of Sciences Grants LP2013–57 (to A. R.) and LP-006/2011 (to M. K.), the Swedish Research Council (to G. K.), the MedInProt Program of the Hungarian Academy of Sciences, the European Union, and the European Social Fund Grant (TÁMOP 4.2.1./B-09/KMR-2010-0003). The authors declare that they have no conflicts of interest with the contents of this article.

[◆] This article was selected as a Paper of the Week.

The atomic coordinates and structure factors (codes 5CSF, 5CSI, 5CSJ, and 5CSN) have been deposited in the Protein Data Bank (http://wwpdb.org/).

Submitted to the BMRB Database under code 25873.

[1] To whom correspondence may be addressed: Institute of Enzymology, Research Center for Natural Sciences, Hungarian Academy of Sciences, Magyar Tudosok Korutja 2, 1117 Budapest, Hungary. Tel.: 36-1-3826613; E-mail: remenyi.attila@ttk.mta.hu.

[2] To whom correspondence may be addressed: Dept. of Biochemistry, Eötvös Loránd University, Pázmány Péter Sétány 1/C, 1117 Budapest, Hungary. Tel.: 36-1-3812171; Fax: 36-1-3822172; E-mail: nyitray@elte.hu.

[3] The abbreviations used are: CaMK, calcium/calmodulin-dependent protein kinase; CaM, calmodulin; SAXS, small angle x-ray scattering; MAPKAPK, MAPK-activated protein kinase; CTKD, C-terminal CaMK-type domain; NTKD, N-terminal AGC-type kinase domain; HM, hydrophobic motif; AL, activation loop; TEV, tobacco etch virus; TCEP, tris(2-carboxyethyl)phosphine; FP, fluorescence polarization; HSQC, heteronuclear single quantum coherence.

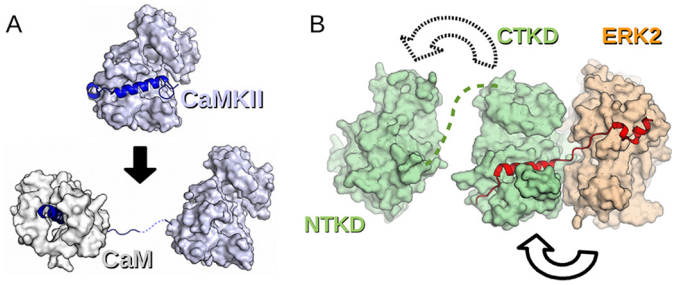

FIGURE 1. **Regulation of CaMK domain containing protein kinase activity.** *A,* inactive CaMKII has an autoinhibitory C-terminal fragment (*blue*) that is released by calmodulin binding (15). Many CaMK-type kinases share an analogous activation mechanism. *B,* RSK1 consists of two kinase domains (*green*) and a flexible C-terminal tail (*red*) (13, 40). ERK2 (*orange*) binds directly to the C-terminal linear motif and phosphorylates the activation loop of the CTKD of RSK1 (which is a CaMK-type kinase domain). Then the CTKD phosphorylates the HM of the NTKD. The phosphorylated HM can anchor the AGC master kinase PDK1, which will, in turn, activate the NTKD.

unknown mechanism (14). Although most MAPKAPK proteins contain a single catalytic domain, the RSK subfamilies are tandem kinases; in addition to their C-terminal CaMK-type domain (CTKD), they have an N-terminal AGC-type kinase domain (NTKD).

The regulatory mechanism of CaMK-type kinases usually involves intracellular Ca^{2+} signals. These kinases have a regulatory C-terminal extension, and in the inactive form the first segment of this tail forms a helical inhibitory helix that blocks substrate or cofactor binding, whereas the second segment is disordered. Upon Ca^{2+} binding, calmodulin (CaM) opens up and binds to the unstructured tail and to the terminal part of the inhibitory helix (15). This interaction remodels the inhibitory segment and brings about an active kinase state (Fig. 1*A*). In contrast, AGC-type kinases have a more complicated regulation mechanism that includes multiple phosphorylation steps. They also have a C-terminal regulatory element that includes two short sequence motifs as follows: the turn motif and the hydrophobic motif (HM). Upstream kinases phosphorylate the HM and turn motif, which will bind to the N-lobe of the kinase domain. Phospho-HM binding remodels the allosteric αC helix of the kinase domain, which in turn activates the kinase, although phospho-turn motif will increase HM binding (16). Fully active kinase requires another phosphorylation on its AL. In some cases phospho-HM also has a binding partner in *trans*; it can bind to an AGC master kinase, for example phosphoinositide-dependent kinase 1 (PDK1), which will then phosphorylate the AL (17).

Phosphorylation on the CaMK-type domain of RSK1 by activated ERK2 sets off the full multistep activation of RSK1 (Fig. 1*B*). In RSK1, the only known role of the C-terminal CaMK-type kinase domain (CTKD) is the phosphorylation of the regulatory hydrophobic motif of the NTKD (18). The phospho-HM of NTKD serves as an anchor motif for PDK1, which will eventually phosphorylate the activation loop of NTKD, resulting in an active kinase that can now phosphorylate a diverse set of substrates downstream of RSK1 (17).

S100B binding to the CTKD of RSK1 may be intuitively similar to typical CaMK activation. Inactive CaMKII has a very similar structure to RSK1; moreover, both the structure and function of S100B are analogous to that of calmodulin. In this study, we have performed biochemical and structural characterization of S100B binding to RSK1. We show that S100B binds to a C-terminal RSK1 segment that is required not only for ERK2 recruitment but also for the autoinhibition of the RSK1 CaMK-type domain. Interestingly, S100B not only directly interferes with the assembly of the ERK2-RSK1 heterodimeric complex, it also negatively affects the activity of the CaMK-type domain of RSK1. The structural basis for this unusual dual-inhibitory mechanism was revealed by combining high resolution x-ray crystallographic analysis with lower resolution solution small angle x-ray scattering and NMR spectroscopy studies on a minimal S100B-RSK1 complex. This analysis revealed a highly dynamic, fuzzy complex (19). We also found that a single RSK1 fragment binds to an S100B dimer, which is rather unusual in the symmetric homodimer-forming S100 protein family (3). Kinetic studies indicated that S100B binding to the CaMK-type domain involves both a conformational selection and an induced fit step. Based on the results of our structural analysis, it was possible to assign a structural state to all observed kinetic steps. Overall, our study gives a detailed biochemical insight into the S100B-RSK1 interaction and could facilitate future drug design studies to treat malignant melanomas.

Experimental Procedures

Protein/Peptide Expression and Purification—The cDNA of S100 proteins, the $RSK1_{CTKD}$ construct containing the C-terminal RSK1 region between residues 411 and 735, as well as different peptides from RSK1 were cloned into modified pET expression vectors. All protein constructs were expressed in *Escherichia coli* Rosetta (DE3) pLysS (Novagen) cells with standard techniques. $RSK1_{CTKD}$ was expressed as N-terminal GST fusion protein with a C-terminal non-cleavable hexahistidine tag. S100B/A4/A2/P/A10 was cloned with an N-terminal TEV-cleavable hexahistidine tag. All peptides were cloned with an N-terminal GST fusion tag. For labeling, the peptide 689–735 contained an N-terminal Cys residue. The shorter reporter peptide (residues 712–735) was chemically synthesized and was N-terminally labeled with carboxyfluorescein. The RSK1 HM construct (AGAHQLFRGFSFVATG) was expressed as an N-terminal GST fusion protein with a C-terminal non-cleavable hexahistidine tag. S100B/A4/A2/P was purified with a nickel-affinity column and cleaved by TEV protease. After complete cleavage, S100B/A4/A2/P was supplemented with Ca^{2+}/Zn^{2+} and injected into a phenyl-Sepharose column. Elution was done with 5 mM EDTA, and the eluted fractions were dialyzed against a Ca^{2+}/Zn^{2+}-containing buffer. After cleavage, S100A10 was further purified by cation exchange chromatography. For biochemical measurements, double affinity-purified RSK1 was used. For SAXS measurement, this double-purified RSK1 was cleaved by the TEV protease, and the sample was further purified on a HiTrap Blue-Sepharose column (GE Healthcare), and then it was complexed with S100B. Peptides were captured by GST affinity purification. After TEV cleavage, GST and TEV were precipitated by boiling the sample. The protein precipitation was spun down, and the supernatant was further purified by reverse-phase HPLC on a Jupiter 300 C5 column (Phenomenex). After lyophilization, the pep-

TABLE 1
Data collection and refinement statistics
Data were collected on single crystals.

	Crystal structure A, S100B-RSK1(683–735)	Crystal structure A′, S100B-RSK1(689–735)	Crystal structure B, S100B-RSK1(696–735)	Crystal structure C, S100B-RSK1(683–720)
Data collection				
Wavelength (Å)	1.0000	0.9730	0.9677	0.9677
Space group	$P2_12_12_1$	$P2_12_12_1$	$P2_12_12_1$	$P2_12_12_1$
Cell dimensions				
a, *b*, *c* (Å)	38.30, 39.24, 172.82	38.31, 38.57, 173.41	37.96, 68.93, 91.49	36.79, 39.93, 178.34
α, β, γ (°)	90.0, 90.0, 90.0	90.0, 90.0, 90.0	90.0, 90.0, 90.0	90.0, 90.0, 90.0
Resolution (Å)[a]	43.20–2.40 (2.46–2.40)	37.65–2.13 (2.19–2.13)	38.12–2.70 (2.77–2.70)	44.59–2.95 (3.03–2.95)
$CC_{1/2}$[a]	100.0 (89.4)	100.0 (93.2)	99.5 (71.6)	99.9 (63.8)
R_{sym}[a]	3.8 (54.9)	5.5 (82.8)	27.0 (164.6)	15.5 (212.6)
Mean $I/\sigma I$[a]	18.69 (2.06)	18.77 (2.07)	9.19 (2.19)	15.85 (1.8)
Completeness (%)[a]	99.1 (99.2)	99.9 (100)	99.9 (100)	99.9 (100)
Redundancy[a]	4.34 (3.30)	6.43 (6.73)	12.30 (13.08)	17.32 (17.81)
No. of reflections[a]	10,773 (774)	15,160 (1064)	7001 (494)	6056 (444)
Refinement				
R_{work}/ R_{free}	0.2432/0.2907	0.2048/0.2500	0.2034/0.2764	0.2514/0.2785
No. of atoms				
All	1512	1568	1570	1576
Ion	4	4	5	4
Water	4	40	14	
B-factors				
All	76.3	68.2	53.7	89.0
Ion	71.9	56.6	45.4	93.8
Water	70.7	53.5	50.0	
Root mean square deviations				
Bond lengths (Å)	0.009	0.007	0.022	0.011
Bond angles (°)	1.245	0.930	1.376	0.849
PDB codes	5CSF	5CSI	5CSJ	5CSN

[a] The highest resolution shell is shown in parentheses.

tides were dissolved in water. For NMR experiments, the ^{15}N-labeled peptide was produced similarly, but before induction, cells were transferred to a $^{15}NH_4Cl$-containing minimal medium. Labeling of cysteine-containing peptides was carried out using 5-(iodoacetamido)fluorescein (Sigma), and the reaction mixture was also purified by HPLC. HM peptide was prepared by double affinity purification.

Crystallization, Data Collection, and Structural Determination—Crystallization samples contained 1 mM S100B monomer and 2-fold excess (~1 mM) of RSK1 peptide in each case. Crystallization was done in a standard sitting drop vapor-diffusion setup at 23 °C. The crystallization solution consisted of 0.1 M HEPES, pH 7, 150 mM NaCl, 20% PEG6000 in all four cases. Crystals were supplemented with 10% glycerol before flash-cooling in liquid nitrogen. Data were collected on the PXIII beamline of the Swiss Light Source (Villigen) and on the ID23 and ID30 beamlines of ESRF (Grenoble, France) at 100 K (Table 1). Data were processed with XDS. Matthews probability calculations indicate the highest probability of an asymmetric complex forming between a single dimer of S100B and a single RSK1 peptide in all crystal forms (20). This was later confirmed after the phase problem was solved by molecular replacement in PHASER with a high resolution structure of S100B as a searching model (21–23). The molecular replacement search identified a single S100B dimer in the asymmetric unit in all cases. Structure refinement was carried out in PHENIX, and structure remodeling/building was done in Coot (24, 25). The final model was refined to 2.4 Å resolution for crystal structure A (with peptide 683–735), to 2.13 Å resolution for crystal structure A′ (with peptide 689–735), to 2.7 Å resolution for the crystal structure B (with peptide 696–735), and to 2.95 Å resolution for the crystal structure C (with peptide 683–720) (Table 1).

Kinase Assays—Activated MAPKs were produced by co-expressing them with constitutively active forms of GST-tagged MAPK kinases in *E. coli* with bicistronic modified pET vectors as described before (13). MAPKs were purified by affinity purification using a HiTrap nickel column (GE Healthcare) followed by ion exchange chromatography on a 1-ml Mono Q column (GE Healthcare). 20 nM activated MAPK was incubated with 1 μM GST-eluted MAPKAPK substrates at room temperature with increasing amounts of S100B. Kinase reactions were carried out in 50 mM HEPES, pH 7.5, 100 mM NaCl, 5 mM $MgCl_2$, 0.05% IGEPAL, 5% glycerol, 2 mM DTT, 2.5 mM $CaCl_2$, 0.5 mM EGTA in the presence of 250 μM ATP and ~5 μCi of [γ-^{32}P]ATP. For RSK1 HM phosphorylation experiments, first 100 nM activated MAPK was incubated with 0.5 μM GST-eluted MAPKAPK substrates at room temperature for 30 min with 250 μM ATP to fully pre-activate MAPKAPK. Then this *in situ* phosphorylated RSK1 was added to a mixture of 20 μM GST-HM and ~5 μCi of [γ-^{32}P]ATP with increasing amounts of S100B. Reactions were stopped with protein loading sample buffer complemented with 20 mM EDTA, boiled, and then subjected to SDS-PAGE. The gel was dried before analysis by phosphorimaging on a Typhoon Trio+ scanner (GE Healthcare). Rates of ^{32}P incorporation into MAPKAPK substrate bands were obtained by the least squares method using three to five data points from the linear range of kinetic phosphorylation curves. Inhibitory constants were determined by fitting a quadratic equation to the measured initial reaction rates. Note that the presented constants are calculated for a symmetrical binding mode, and therefore they have to be divided by a factor of 2 to get the asymmetrical binding constant.

Binding Assays and Kinetic Measurements—Steady-state tryptophan fluorescence was measured with a Synergy H4

(BioTek Instruments) plate reader in 384-well plates. The excitation wavelength was 295 nm, and the emission was detected at 330 nm. 1 μM GST-RSK1$_{CTKD}$ was mixed with increasing amounts of S100B or CaM. As a negative control, 1 μM GST was also mixed with increasing amounts of S100B (data not shown). Fluorescence intensity change was only observable in the case of RSK1-S100B. The experiment was carried out in triplicate. The measured data were fitted by a quadratic binding equation.

Fast kinetic measurements were performed with the stopped-flow instrument SFM-300 (Bio-Logic) with excitation at 297 nm. Fluorescence emission from Trp residues was observed through a 340-nm bandpass filter (Comar Optics). All reactions were performed at 25 °C in 20 mM Tris, pH 7.5, 100 mM NaCl, 0.5 mM TCEP, 2 mM $CaCl_2$, and 1 mM Ca-EDTA. Post-mixing GST-RSK1$_{CTKD}$ concentration was fixed to 1 μM. Amplitudes and the observed rate constants of double exponential fits were determined using Origin 7 (OriginLab Corp.). To determine the off-rate constants, complex samples were mixed with the RSK1(683–735) peptide.

In direct FP measurements, 50 nM fluorescein-conjugated reporter peptide was mixed with increasing amounts of S100, and the FP signal was measured with a Synergy H4 (BioTek Instruments) plate reader in 384-well plates. In competitive FP measurements 50 nM labeled reporter peptide was mixed with S100 in a concentration to achieve ~60–80% complex formation. Subsequently, increasing amounts of unlabeled peptide or GST-RSK1 constructs were added. In all simple competitive measurements, 20 μM S100B was mixed with labeled peptide. The K_d value for each experiment was determined by fitting the data to a quadratic or a competition binding equation. Titration experiments were carried out in triplicate, and the average FP signal was used for fitting the data with Origin 7.

Gel filtration experiments were carried out using an in-house packed 10/300 Superdex 75 column and GF buffer containing 20 mM Tris, pH 7.5, 150 mM NaCl, 1 mM $CaCl_2$, and 25 μM TCEP. Each sample was injected at least two times into the column. S100B concentration was 1 mM in all cases, which is much higher than the observed dissociation constant.

Secondary and Solution Structure Determination—CD spectroscopy measurements were carried out on a Jasco J-810 spectropolarimeter using a 0.1-mm wide cuvette in a buffer containing 20 mM Tris, pH 7.5, 150 mM NaCl, 2 mM $CaCl_2$, 2 mM Ca-EDTA, and 1 mM TCEP. The free RSK1(683–735) peptide concentration was 50 μM. To obtain the CD spectrum of the S100B-bound peptide, the spectrum of free S100B (120 μM S100B monomer) was subtracted from the spectrum of the protein complex (50 μM peptide and 120 μM S100B monomer) assuming that the secondary structure of S100B does not change upon RSK1(683–735) binding. Each spectrum was measured in triplicate, and the averaged spectra were used for analysis. The subtracted spectra of the free and the bound peptide was fitted with BeStSel (26).

All SAXS measurements were performed at the BM29 beamline at ESRF. Data were analyzed using the ATSAS program package (27). A dilution series of a concentrated sample of the gel filtrated RSK1(683–735)-S100B complex was measured from 8 to 0.4 mg/ml. No concentration effect was observed during the measurement. The primary data analysis was performed in PRIMUS (Fig. 7). The scattering curve was interpreted with CORAL (27). In the CORAL modeling of structure A, 16-residue long N-terminal, 25-residue long linker, and 4-residue long C-terminal regions were modeled to the peptide fragments obtained in the crystal structure (Figs. 6 and 7). Fragments from the crystal structure were treated as rigid bodies, and only the "invisible" flexible elements were modeled. Solution scattering from the RSK1 CTKD construct was determined with on-line size-exclusion chromatography-SAXS using a Superdex 75 column. Fit of the crystal structure was determined by CRYSOL, and an *ab initio* model was generated by 15 independent run of DAMMIN (27). The best fit was achieved by ensemble modeling with EOM, including both ordered and disordered C-terminal tails (Fig. 10) (28). Ensemble modeling with solely ordered or disordered C terminus resulted in worse fit and not reliable models (data not shown).

NMR spectra were recorded on a Bruker Avance III 700 spectrometer operating at 700.17 MHz for ^{1}H, equipped with 5-mm triple-resonance probe head with a *z* axis gradient. The optimal spectral dispersion was achieved at 303 K, and this temperature was selected from a series of HSQC spectra recorded in the 277–320 K range (for both the free and complexed peptide). ^{1}H chemical shifts were referenced to the internal 4,4-dimethyl-4-silapentane-1-sulfonic acid standard, whereas ^{15}N chemical shifts were referenced indirectly via the gyromagnetic ratios. Both samples had the following compositions: ~0.9 mM ^{15}N-labeled peptide, 20 mM MES buffer, pH 6.00, 20 mM NaCl, 3 mM NaN_3, 2 mM TCEP, 5 mM $CaCl_2$ and 10% D_2O. S100B concentration was ~2 mM in the complex. Peak assignment and sequential connectivities were determined from the analysis of standard three-dimensional HSQC-TOCSY and three-dimensional HSQC-NOESY measurements. Spectra were processed with TOPSPIN and analyzed using the CARA (29) software program. Chemical shifts were deposited to the BMRB database under accession number 25873.

Results

S100B Exerts Dual-level Inhibition on ERK2 → RSK1 Activation—To quantitatively characterize the binding of S100B to RSK1$_{CTKD}$, we measured the intrinsic tryptophan fluorescence change of RSK1 upon S100B binding. Because none of the MAPKAPKs can bind to CaM, we used it as a negative control in the experiment. Because neither CaM nor S100B contains a tryptophan residue, the fluorescent signal originates from RSK1. A relatively large intensity decrease (~25%) was found in the presence of large excess of S100B but not in the case of CaM. The measured dissociation constant of the S100B-RSK1$_{CTKD}$ complex was found to be about 5 μM (Fig. 2*A*).

Activated ERK2 can phosphorylate the CTKD of RSK1 on Thr-573 in *in vitro* kinase assays. In turn, activated CTKD can efficiently phosphorylate an HM containing GST fusion protein in *trans* (18). An inhibiting role of S100B on RSK1$_{CTKD}$ phosphorylation has been recently reported (7). We also find that S100B clearly impedes RSK1$_{CTKD}$ phosphorylation by ERK2 in an *in vitro* kinase assay using recombinantly expressed and purified components (Fig. 2*B*). In addition, S100B also blocks the activity of activated RSK1$_{CTKD}$ on an HM-contain-

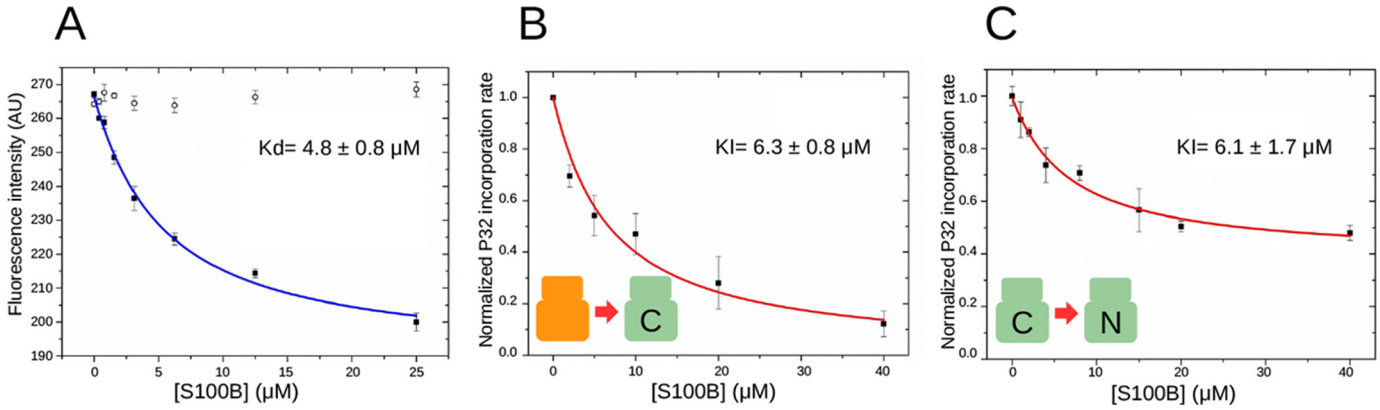

FIGURE 2. **S100B binding inhibits RSK1 activation.** *A,* S100B binding induces a conformational change in GST-RSK1$_{CTKD}$, which can be monitored by the change of intrinsic tryptophan fluorescence. The dissociation constant calculated based on this change is 4.8 μM. CaM is unable to induce a similar effect on RSK1 (*empty circles*). The measurement is representative of at least three sets of independent experiments, and K_d values were calculated from triplicate data points. Triplicates were independently prepared samples that were assayed at the same time. *Error bars* show standard deviation from the mean. *AU*, arbitrary unit. *B,* presence of S100B inhibits CTKD phosphorylation by ERK2 with a K_i = 6.3 μM in an *in vitro* kinase assay. S100B fully inhibits the phosphorylation step between active ERK2 and the CTKD phosphorylation. *C,* presence of S100B also acts as an inhibitor also when an NTKD-HM containing construct is phosphorylated in *trans,* with a K_i = 6.1 μM. Notice that this inhibition is only partial, indicative of a complex inhibitory mechanism on CTKD-mediated phosphorylation on NTKD. *B* and *C* show the mean of three independent reactions, and *error bars* are standard deviation from the mean. Initial rates of ^{32}P incorporation were normalized to reactions where S100B was absent.

ing NTKD substrate fragment in *trans* (Fig. 2*C*). The calculated inhibitory constants were found to be around 6 μM for ERK2 → CTKD signaling, which showed a good agreement with the binding affinity of the S100B-CTKD complex (see above). It is noteworthy that S100B binding did not completely abolish CTKD kinase activity on the NTKD HM fragment but only lowered the reaction rate to ~40% of the original activity under saturating conditions. From these observations, we could rule out that S100B has a CaM-like effect, which is known to exert activation on CaMKII (30). In conclusion, S100B was shown here to be a dual-level specific inhibitor of RSK1 activation, acting both on the ERK2 → CTKD and also on the CTKD → NTKD level.

C-terminal Region of CTKD Mediates High Affinity Binding to S100B—It was proposed that the S100B-RSK1 interaction requires the flexible C terminus of RSK1 (7). Interestingly, ERK2-RSK1 binding also depends on this C-terminal tail (31). These findings suggest that S100B and ERK2 binding to RSK1 is mutually exclusive. To show that the two RSK1-binding partners indeed compete for the same RSK1 region, we used FP-based binding assays with a fluorescently labeled C-terminal fragment of RSK1. Titrating this labeled reporter peptide RSK1(712–735) with S100B in the presence of calcium ions indeed increased its fluorescence anisotropy, indicating direct interaction (Fig. 3*A*). In contrast, in the presence of EDTA (or in the absence of Ca^{2+}) no changes in FP were observed (Fig. 3*B*). Thus, the interaction seemed to be specific; however, the binding affinity was found to be low (K_d = 30 μM). We next extended the length of the reporter peptide toward the N terminus (residues 689–735). The binding affinity of this extended peptide, including the inhibitory helix region (αL) as well, was found to be about 6-fold higher compared with the shorter RSK1 peptide (Fig. 3*C*).

FP-based binding measurements can also be used to determine the binding affinities of unlabeled constructs. The dissociation constant of the RSK1$_{CTKD}$ protein as well as different RSK1 C-terminal fragments were measured in competition assays. The binding affinity of RSK1$_{CTKD}$ determined in this assay (4 μM) was similarly in the low micromolar range as the affinity measured by the assay based on monitoring the tryptophan fluorescence change upon S100B binding (Fig. 3*D*). Extending the peptide length to the end of the core kinase domain of CTKD(683–735) greatly increased the strength of complex formation (K_d = 40 nM) (Fig. 3, *E* and *F*). For this high affinity complex, the binding stoichiometry can be determined from the competition curve. In the presence of 20 μM S100B, maximal signal decrease was observed around 10 μM unlabeled RSK1(683–735) peptide, indicating an asymmetrical binding mode. This asymmetry means that a single RSK1(683–735) peptide binds to one S100B dimer. A similar 1:2 binding stoichiometry was observed in the complex of non-muscle myosin IIA and S100A4, but it has not been previously observed in any S100B complex (3). To further confirm the 1:2 binding ratio, we examined the complex formation in gel-filtration experiments. Free S100B dimer and free RSK1(683–735) peptides have different elution volumes, and a slight upward shift in the elution volume is apparent when both components are added, which is suggestive for complex formation. Mixing the partners in a 1:2 molar ratio gives a homogeneous fast eluting peak, whereas adding equimolar RSK1(683–735) peptide to S100B chains (2:2 ratio) results in a mixture of the previously identified complex and free RSK1 peptide (Fig. 3*G*).

S100 proteins are structurally highly homologous, and therefore it is important to determine whether the S100B-RSK1 interaction is specific within the S100 family. Direct binding between the RSK1(683–735) peptide and S100B, S100A4, S100A2, and S100P was observed by FP-based binding experiments. Nevertheless, it was found that only S100B was able to mediate high affinity binding with the RSK1$_{CTKD}$ (Figs. 3*H* and 4). This result suggests that after anchoring itself to the C-terminal region of RSK1, S100B may form additional specific interactions with the kinase domain itself. In summary, the RSK1-S100B interaction seems to be specific among S100 protein family members.

The short labeled RSK1(712–735) peptide has a marginal affinity (30 μM) toward S100B; however, it can form a high affinity complex with ERK2 (0.5–1 μM). This phenomenon can be exploited to investigate co-binding of ERK2 and S100B to RSK1. At high S100B concentration, ERK2-RSK1(712–735) complex formation could still be measured both in the presence or the absence of calcium ions in direct FP measurements (Fig. 3*I*). In competitive titration experiments using the RSK1(689–735) peptide fragment, which is a much better S100B binder, we could measure the effect of active/inactive S100B on ERK2-RSK1(689–735) complex formation. If co-binding can occur then almost identical competitive titration curves are expected. However, if there is a competition between ERK2 and S100B then one can measure an increase in the observed dissociation constant for the ERK2-RSK1 binding event. The measured affinity indeed decreased

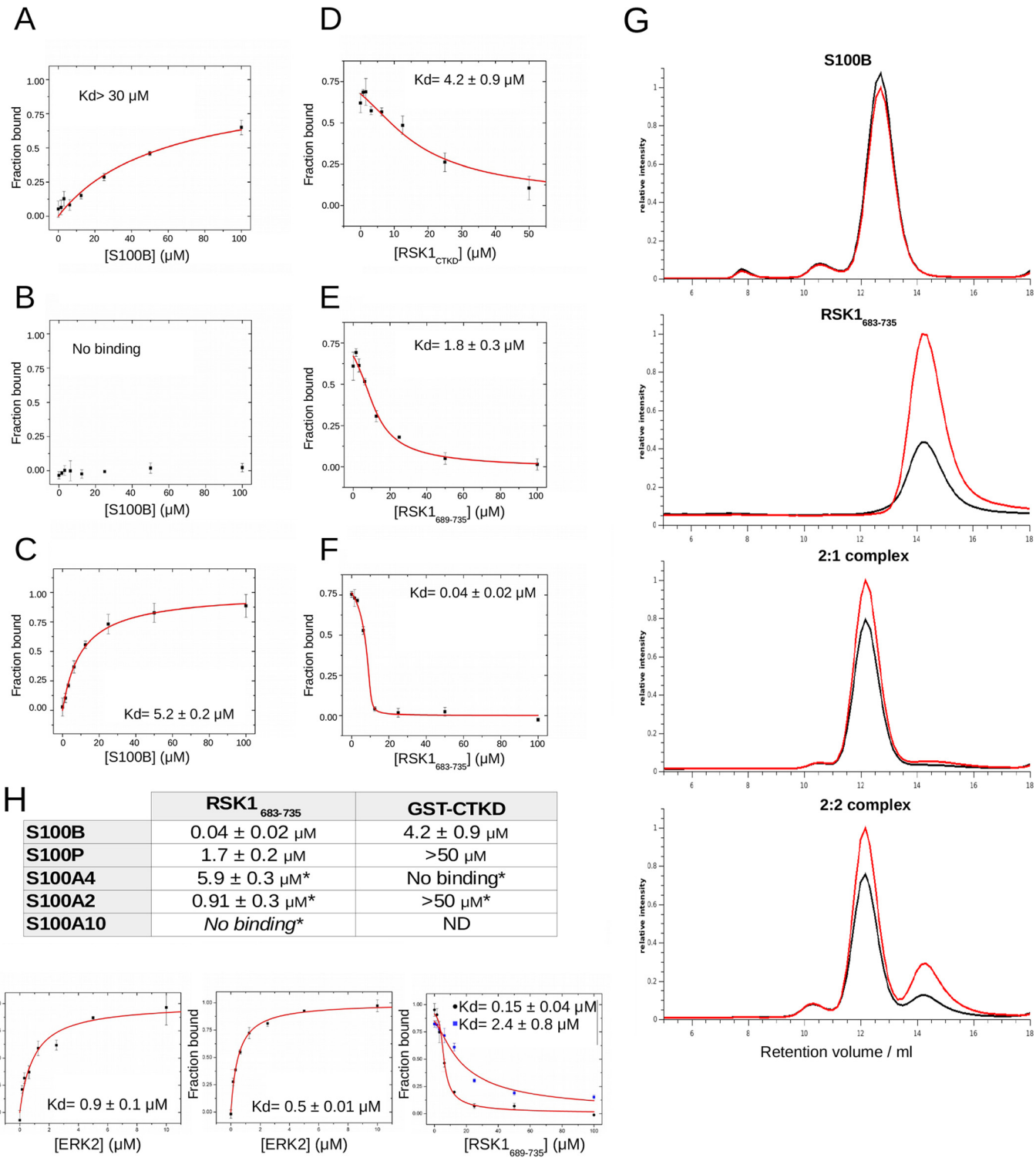

H

	RSK1 683-735	GST-CTKD
S100B	0.04 ± 0.02 μM	4.2 ± 0.9 μM
S100P	1.7 ± 0.2 μM	>50 μM
S100A4	5.9 ± 0.3 μM*	No binding*
S100A2	0.91 ± 0.3 μM*	>50 μM*
S100A10	*No binding**	ND

by about 1 order of magnitude (Fig. 3*I*). This result indicates that there is a direct competition for the RSK1 tailpiece between the two binding partners.

Crystal and Solution Structure of the Minimal RSK1-S100B Complex—For structural studies, a set of RSK1 peptides with various deletions both from the C- and N-terminal ends of RSK1(683–735) were made (Figs. 4 and 5*A*). We found that if either the C- or the N-terminal part was truncated, the binding affinity decreased. To visualize the atomic details of the minimized RSK1-S100B interaction, we determined the crystal structure of the high affinity RSK1(683–735)-S100B complex (crystal structure A). Unfortunately, only a small N- and C-terminal portion of RSK1 could be built in the crystallographic model; nonetheless, the structure verified the asymmetric nature of the complex (Fig. 5, *B* and *C*). To improve the quality of the crystal structure, we attempted protein crystallization with truncated peptide constructs to decrease the conformational flexibility. An N-terminally truncated peptide (RSK1(689–735)) gave a very similar crystal structure but with better resolution and a more interpretable electron density map (crystal structure A′) (Fig. 5*D*). A non-isomorphous crystal formed with a yet shorter peptide (696–735; crystal structure B), whereas a nearly isomorphous crystal was obtained with the peptide 683–720 (crystal structure C) (Fig. 5*C*). Comparison of these four structures suggests that the crystallographic models likely captured different conformations of the interaction (Fig. 5*D*). In crystal structure B, the middle part of the RSK1 peptide was also missing, but the C-terminal part showed helical structure. Similarly to structure A, only the two classical S100 binding pockets were occupied by the terminal regions of the RSK1 peptide. Structure C displayed a very different structure for the bound RSK1 peptide. For this peptide (683–720), in agreement with its lower affinity compared with the full-length peptide (residues 683–735) or the N-terminally truncated peptide (residues 696–735), one of the two canonical pockets was unoccupied. However, a helical segment from the peptide was found in the non-conventional binding site of S100B, which is a shallow groove connecting the two canonical sites as described in Ref. 3.

In structure B, the second canonical S100 binding interface interacts with a C-terminal helical element of RSK1. This region of RSK1 has helical propensity in solution and also it forms a helix when it is bound in the ERK2 docking groove (13). Moreover, the helical element from structure C was found to be analogous to the surface-oriented side of the bound inhibitory helix of the previously solved RSK1 structures (Fig. 5*C*) (13, 14, 32). We propose that structure C captured the S100B-RSK1 complex in a state where the interaction between the S100B and the RSK1 C-terminal segment may be such as in an S100 inhibited complex with full-length RSK1. Superimposing the S100B complex with an inhibited RSK1 structure via this helical element (between residues 700 and 707 with a root mean square deviation of 1.1 Å for 51 atoms) suggests that the S100B dimer could help locking the inhibitory helix in its position, and thus promote its interaction with the core kinase domain while it simultaneously blocks MAPK binding through the secondary classical S100-binding interface (Fig. 5*E*). However, it should be noted that atomic clashes are apparent between S100B and the αG helix of RSK1 in a model generated by this simple superimposition. Thus, the αG helix must undergo some kind of structural rearrangement upon S100B binding to be compatible with the binding mode that was observed in the crystallographic model C.

All crystal structures included a segment of the αL helix (between residues 697 and 701) on the N-terminal binding side that is in coil conformation. This apparently key interaction however does not contain any directed bonds toward S100B. In structure A, A′, and B, the C-terminal binding side is occupied by the MAPK-binding basic motif with different conformations. Interestingly, in structure B this segment was helical just as in the case of the MAPK-bound conformation. This interaction is responsible for the direct competition with ERK2 binding. In structure C, where this basic motif was truncated, a helical element appeared next to the N-terminal binding side. Because different regions showed helical propensity in our crystal structures, we wanted to investigate the secondary structure of the bound RSK1(683–735) peptide. We measured the solution structure using CD spectroscopy (Fig. 6*A*). The free peptide is highly flexible and lacks any secondary structural element, but the bound form contains a single ~12-amino acid-long helical element. For the other characterized asymmetric S100-binding partner (NMIIA), a much larger helical content was calculated (>60%, ~20 residues long) by an identical method, which was later also confirmed by high resolution crystal and solution structures (3, 4). This suggests that the RSK1 binding mode to S100B is different from the NMIIA binding to S100A4. In addition, these data also suggest that

FIGURE 3. **Characterization of RSK1 C-terminal region as the interaction hot spot for S100B binding.** *A,* MAPK binding C-terminal peptide (RSK1(712–735)) binds weakly to S100B ($K_d \approx 30$ μM). *B,* in the absence of Ca^{2+}, this interaction is abolished indicating specific binding toward S100B. *C,* longer C-terminal fragment, including the inhibitor helix (RSK1(689–735)), bound markedly stronger ($K_d = 5.2$ μM). This labeled peptide was used to measure competitive binding of unlabeled peptides in further experiments. *D,* GST-$RSK1_{CTKD}$ competed with the labeled long peptide with a K_d of 4.2 μM. *E,* unlabeled RSK1(689–735) bound somewhat stronger ($K_d = 1.8$ μM). *F,* extending this peptide to include the full C-terminal extension of RSK1(683–735), which now also included an extension before αL, increased the binding affinity 2 orders of magnitude ($K_d = 0.04$ μM). The shape of the curve indicates asymmetric (2:1) binding because the S100B concentration was 20 μM. Each measurement is representative of at least two sets of independent experiments where K_d values were calculated from triplicate data points. Triplicates were independently prepared samples that were assayed at the same time. *Error bars* show standard deviation from the mean. *G,* gel filtration experiments validated the asymmetric 2:1 stoichiometry in solution. The *upper two panels* show chromatograms of S100B and peptide samples. The *lower panels* show chromatograms of S100B and RSK1 peptide complexes with a mixed stoichiometry of 2:1 and 2:2. Notice that the peak corresponding to the free peptide appears only at 2:2 mixing ratio. The panel shows normalized intensity computed according to the maximal absorption at 280 nm (absorption at 260 nm is colored in *black* and at 280 nm is colored in *red*). *H,* summary of binding affinities between different S100 proteins and RSK1 constructs. (*Asterisks* indicate that the fluorescent reporter was a labeled peptide from p53 (p53(17–56)), which is an S100 interaction partner (41). The RSK1-based reporter peptide was used for S100B and S100P measurements.) (See Fig. 4 for details.) *I,* S100B and ERK2 binding to RSK1 is not independent. Using the fluorescent reporter RSK1(711–735), it is possible to measure only the ERK2-RSK1 binding in the presence of active/inactive S100B. Binding curves in the presence of 2 mM Ca^{2+} (*left*) and 5 mM EDTA (*middle*) show very similar binding. Competitive binding experiment with a longer peptide (RSK1(689–735)) showed that the binding curves in the presence or absence (*black*) of Ca^{2+} are clearly different without or in the presence of 10 times molar excess of S100B (*right*). A clear decrease in the interaction strength of ERK2-RSK1 binding indicates that ERK2 and S100B binding to RSK1 is mutually exclusive.

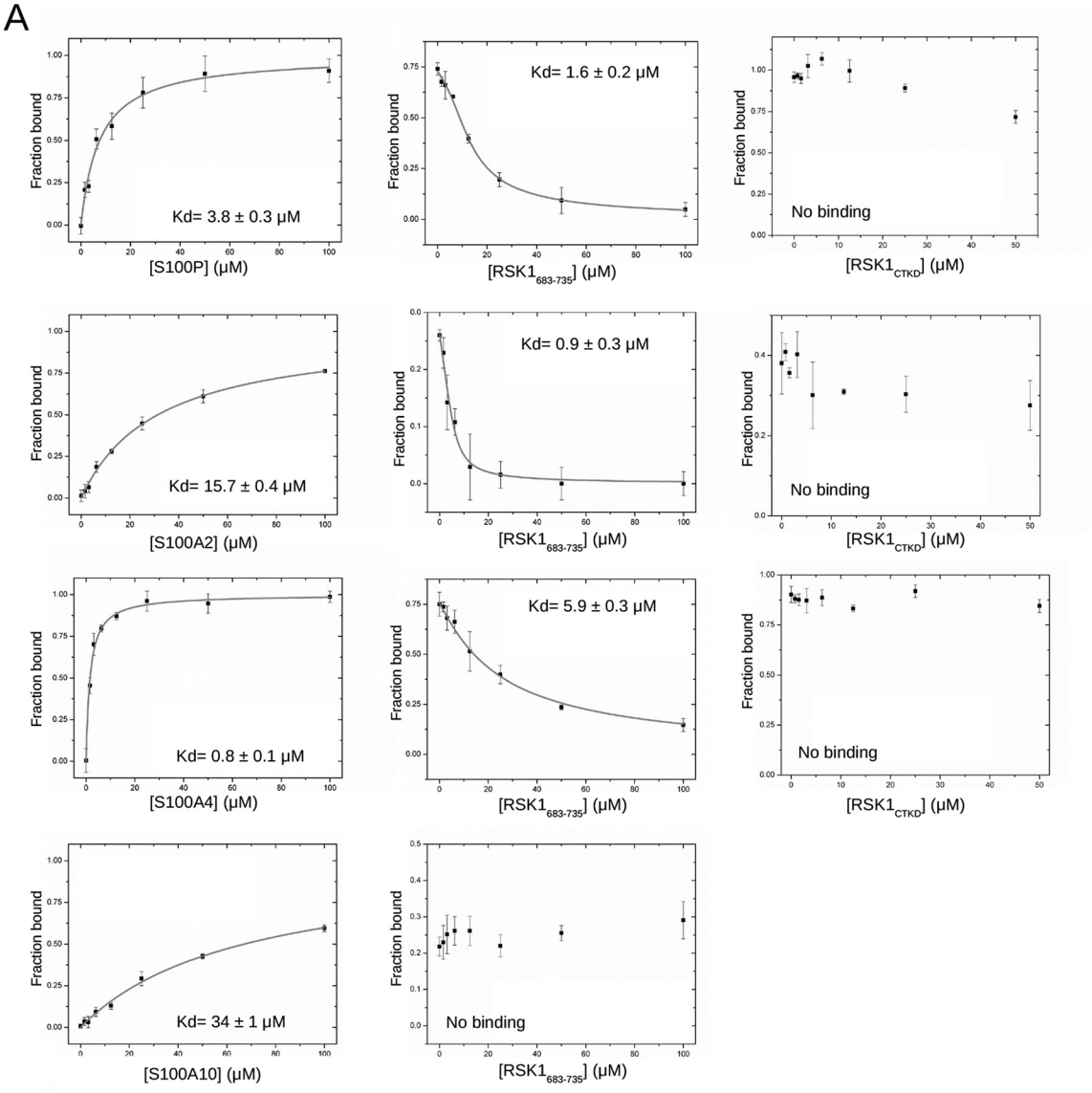
A
Fraction bound
Kd= 3.8 ± 0.3 μM
[S100P] (μM)
Kd= 1.6 ± 0.2 μM
[RSK1683-735] (μM)
No binding
[RSK1CTKD] (μM)
Kd= 15.7 ± 0.4 μM
[S100A2] (μM)
Kd= 0.9 ± 0.3 μM
[RSK1683-735] (μM)
No binding
[RSK1CTKD] (μM)
Kd= 0.8 ± 0.1 μM
[S100A4] (μM)
Kd= 5.9 ± 0.3 μM
[RSK1683-735] (μM)
No binding
[RSK1CTKD] (μM)
Kd= 34 ± 1 μM
[S100A10] (μM)
No binding
[RSK1683-735] (μM)

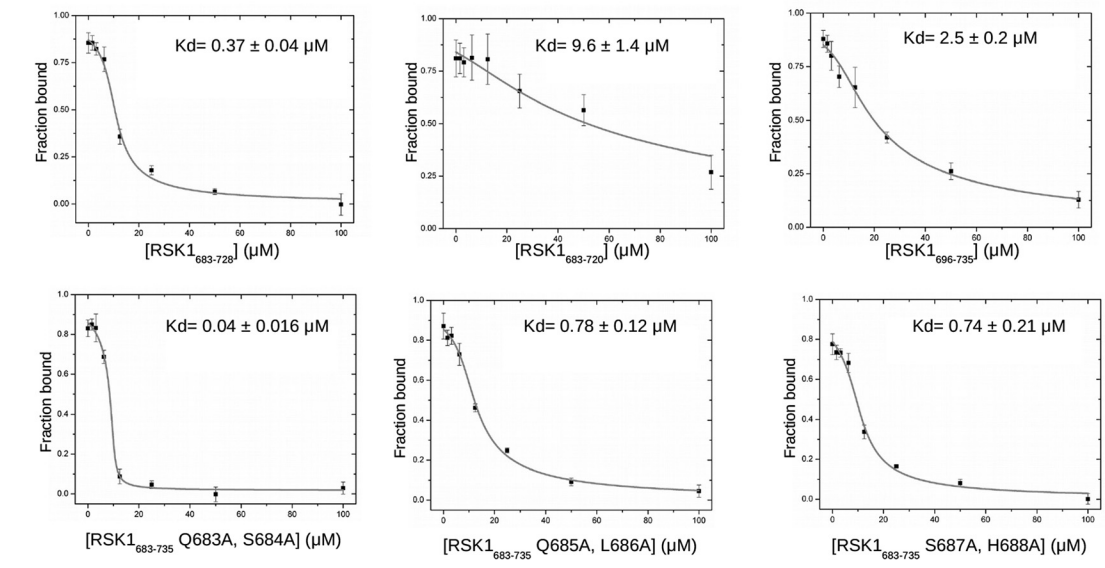
B
Fraction bound
Kd= 0.37 ± 0.04 μM
[RSK1683-728] (μM)
Kd= 9.6 ± 1.4 μM
[RSK1683-720] (μM)
Kd= 2.5 ± 0.2 μM
[RSK1696-735] (μM)
Kd= 0.04 ± 0.016 μM
[RSK1683-735 Q683A, S684A] (μM)
Kd= 0.78 ± 0.12 μM
[RSK1683-735 Q685A, L686A] (μM)
Kd= 0.74 ± 0.21 μM
[RSK1683-735 S687A, H688A] (μM)

either of the two observed helical element is compatible with the observed total helical content, but both cannot exist at the same time.

Based on our multiple crystallographic models, it appears that the S100B-RSK1 complex can acquire many possible structural states. The first model is based on crystal structures A and A′; both canonical binding pockets are filled with the N- and C-terminal part of the linear motif adopting a coil structure. The second model is based on crystal structure B; the N-terminal binding region is in coil conformation, but the C-terminal is helical. The last two possible models are based on structure C. In these complexes, the N-terminal part is in coil, but it is extended by a helical intervening part, and the C-terminal binding region may bind as it is seen in either the A (or A′) or the B crystal structure. Because we wanted to further analyze this structurally diverse, apparently fuzzy complex, as revealed by x-ray crystallographic analysis, we used SAXS to obtain at least low resolution structural information about the shape of the complex in solution. We were able to measure high quality SAXS from an isolated complex with the RSK1(683–735) peptide (Fig. 7). In all crystal structures, only small peptide fragments could be located in the electron density. Using SAXS data, however, we could simulate the whole complex using the above described four templates (Fig. 6*B*). In these simulations the "crystallographically" invisible parts were *ab initio* modeled using a program called CORAL (27). Out of the four structural models, only the first one (based on structure A and A′) fit the obtained SAXS curve, and therefore this describes the solution structure of the RSK1-S100B complex the best (Figs. 6 and 7). The simulated models have high flexibility between the two anchor positions; therefore, it can be considered as a clamp-type fuzzy complex (19). From 10 independent simulations, two types of clusters were observed as follows: one with a free and one with an S100-bound N-terminal part (Fig. 7). This N-terminal flanking segment seems to be responsible for a large increase in the binding affinity (Figs. 4 and 5*A*). Unfortunately, this site on S100B is close to a crystal packing interaction surface; therefore, this additional interaction remains hidden in our crystal structures. To further characterize this flanking element, we performed mutational scanning on the first six residues (Figs. 4 and 5*A*). We found that the first two residues do not directly contribute to the binding, but if either residues 685–686 or 687–688 were mutated to Ala, the binding affinity decreased with an order of magnitude. We assume that the hydrophobic Leu-686 and basic His-688 are most likely the key residues determining the high affinity binding of RSK1(683–735) to S100B.

As an additional analysis, we measured the changes in the solution structure of this minimal RSK1 peptide by NMR spectroscopy. We characterized the RSK1(683–735) peptide in free form and performed peak assignment at 303 K from the three-dimensional TOCSY-HSQC and NOESY-HSQC measurements. Already the narrow signal dispersion of the HSQC spectrum informed us about the disordered nature of this free RSK1 tail fragment. Addition of excess S100B under identical conditions resulted in changes in the spectrum (Fig. 7*E*). The complex had an increased molecular mass and as a consequence a different tumbling time in solution. As changes were monitored from the ^{15}N RSK1 peptide side (S100B protein was unlabeled), the consequence of complex formation would be observable as shifted and broadened peaks and also peaks broadened below the detection limit in the HSQC spectrum.

Unfortunately, we were unable to assign the complex spectrum under these experimental conditions. Nevertheless, if we assume that close peaks in the HSQC spectra correspond to the same amino acid, we could gain residue level information of the changes in the chemical environment of the RSK1 peptide upon complex formation. Based on the overlay of the spectra, it appears that many peaks showed no or little chemical shift changes. These are the residues that belong to the N-terminal flanking and the intervening parts (for example Val-694, Gly-696, Ser-707, and Lys-709 remained mostly unchanged, see Fig. 5). Although 54 peaks (including minor peaks) were detectable for the free peptide, only 47 peaks were present in the spectrum of the complex (Fig. 7*E*). Disappearing peaks correspond to residues involved in direct binding interaction with intermediate exchange. However, these resonances can also belong to the shifted, newly appearing broad peaks. These changes clearly affect the C-terminal binding side (residues 724–730) and residues from the N-terminal side (like Ala-697 or Ala-704); they are in full accordance with the crystallographic model (Fig. 5) and indicating that these regions could provide the "clamps" of the fuzzy complex. In addition, the N-terminal flanking part was also changed upon binding (*e.g.* Leu-686). The lack of dramatic changes in signal dispersion upon complex formation suggests that there are no new secondary structural elements forming in the RSK1 peptide. This suggests that the observed helical content by CD spectroscopy is due to transient helix formation. Overall, these observations corroborate the existence of a fuzzy complex and are in agreement with the crystallographic analysis of the RSK1-S100B complex.

Rapid Kinetic Experiments Reveal That S100B Binding to RSK1 Involves Both Conformational Selection and Induced Fit—The inherent tryptophan fluorescence change of RSK1 upon S100B binding (Fig. 2*A*) could be used to decipher the kinetic mechanism of the interaction. In stopped-flow experiments, we were able to follow RSK1-S100B complex formation in real time by mixing RSK1 with S100B as well as to monitor its dissociation by mixing the complex with a "chaser" peptide from RSK1 (Fig. 8). Both the observed association and dissociation transients could be fitted by double exponential functions. The observed rate constants of the first and second

FIGURE 4. **Fits of the fluorescence polarization binding measurements.** *A,* direct (*left*) and competitive (*middle, right*) FP measurements for different S100 proteins. In competitive experiments, unlabeled RSK1(683–735) (*middle*) or RSK1$_{CTKD}$ (*right*) was used as a competitor. In experiments with S100A2, S100A4, and S100A10, a fluorescein-labeled p53 reporter peptide (p53(17–56)) was used as a reporter peptide. *B,* competitive FP measurements with unlabeled truncated or mutated RSK1 peptides using the S100B-RSK1 peptide reporter system. Titration experiments without fits to a direct or a competitive binding equation did not show binding or complete competition with the labeled reporter peptide, which was regarded as an indication for nonspecific binding. Each measurement is representative of at least two sets of independent experiments where K_d values were calculated from triplicate data points. Triplicates were independently prepared samples that were assayed at the same time. *Error bars* show standard deviation from the mean.

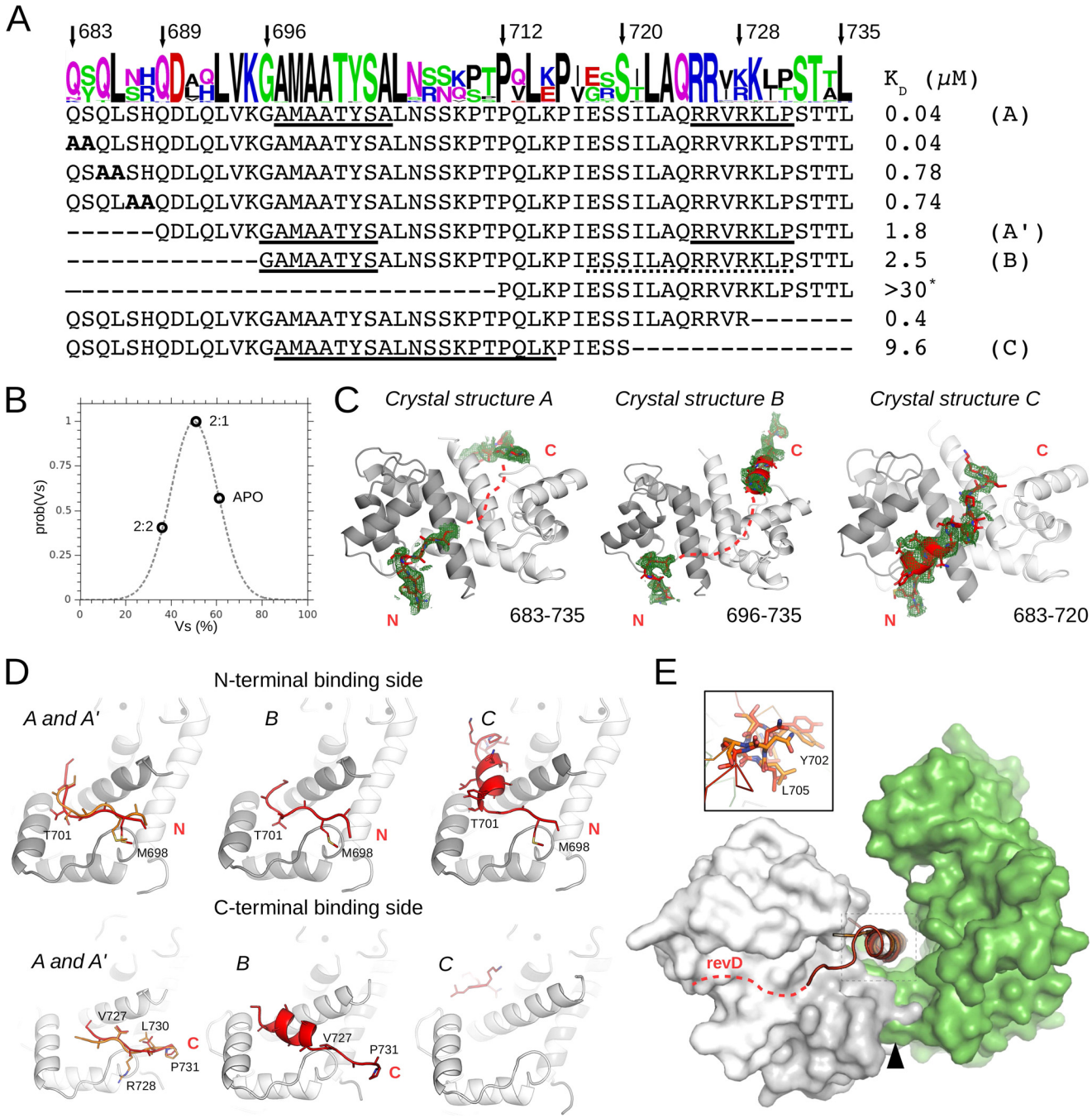

FIGURE 5. **Structural properties of the S100B-RSK1 complex.** *A,* summary of binding affinities between S100B and various truncated RSK1 peptide constructs. (See Fig. 3 and 4 for details.) Removal of small regions at both sides greatly influences the binding affinity. The sequence logo was generated by using vertebrate ($n = 40$, non-redundant) RSK1/2 sequences. Point mutations are *highlighted* in the sequence. The *underlined* sequences were modeled into the corresponding complex crystal structure, although others could not be built in. *Dotted lines* indicate some register ambiguity in the interpretation of the corresponding crystallographic model. In the autoinhibited MAPK-bound state residues between 690 and 707 form the αL helix, and the C-terminal tail from 712 is involved in MAPK binding (13). *B,* Matthews probabilities of crystal structure A calculated for apo-S100B and for 2:1 and 2:2 complexes (20). In all determined structures the 2:1 complex was the most preferred content. *C,* F_oF_c simulated annealing omit map (contoured at 2σ) around the RSK1 peptides (*red*) for the determined crystal structures A, B, and C. The S100 monomers are shown in *gray* or *light gray* schematic representation. Both docking pockets of the S100B are filled by the N- and C-terminal fragments of the RSK1 peptide in structure A, A′, and B; however, only the N-terminal part along with a helical extension is present in structure C. *D,* detailed view of the observed N- and C-terminal parts of the presented structural states. The N-terminal binding mode in structure A and B is highly similar. Bound calcium ions are shown with *black spheres*. The binding fragments from structure A′ is colored in *orange*. *E,* crystal structure C can be superimposed to an inactive $RSK1_{CTKD}$ structure (*green*) via their common helical region (*red*). (*revD*: the docking motif for ERK2). The *inset* shows that S100B binds to the solvent-accessible side of the inhibitor helix (αL). *Black arrow* indicates steric clash between the αG helix of RSK1 and the superimposed S100B.

phases of the association transients showed a decreasing and an increasing tendency, respectively, with increasing S100B concentration. The rate constants of both phases reached saturation at a relatively low S100B concentration (Fig. 8, *C* and *D*). These profiles are indicative of the presence of both conformational selection (first phase) and induced fit (second phase) pro-

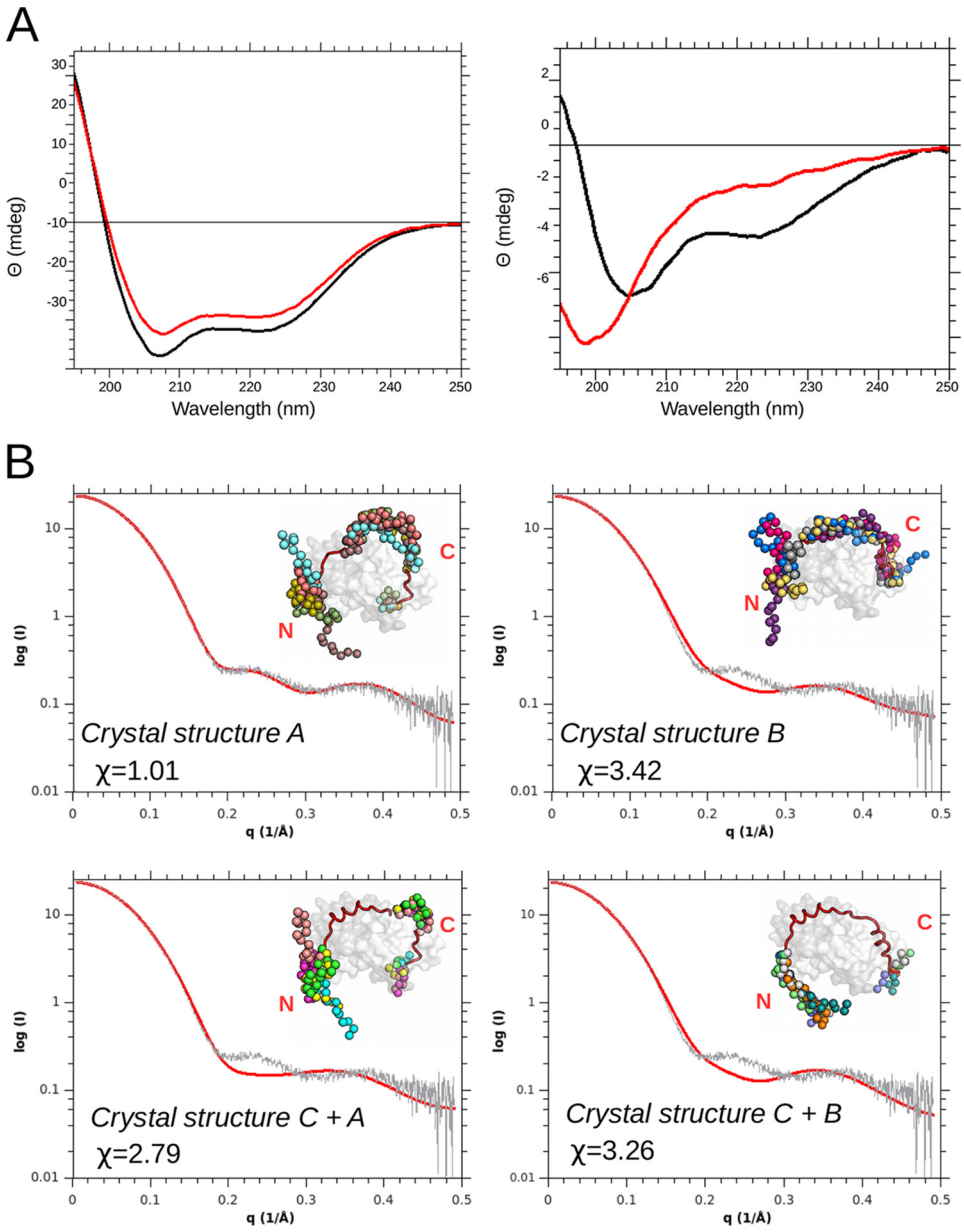

FIGURE 6. **Solution structure of the S100B-RSK1 complex.** *A,* CD spectra of free (*red*) and RSK1(683–735)-bound (*black*) S100B is shown on the *left side* and the CD spectra of free (*red*) and S100B-bound (*black*) RSK1(683–735) peptide is shown on the *right side*. An increase in the helical content upon complex formation can be observed without major changes in the S100B structure itself. Deconvolution of the difference spectra by the program BeStSel reveals an ~13-amino acid-long single helix in the bound state (the free peptide is completely disordered) (25). *B,* based on the crystallographic models, using two N- and two C-terminal RSK1-interacting fragments, four types of S100B-RSK$_1$(683–735) complexes can be constructed. Each model was refined against high quality SAXS data, but only one of the models, corresponding to crystal structure A, matched the experimental SAXS curve (Fig. 7). The best fit from 10 independent CORAL simulations is shown along with a superposition of five randomly chosen simulated structures. For simulations, flexible parts were modeled and are shown here with *spheres*, whereas the rest was treated as rigid.

cesses. As dissociation was dependent on chaser peptide concentration, dissociation rate constants were determined by linear extrapolation to zero chaser concentration (Fig. 8, *G* and *H*). Based on the exponential approximations (Fig. 8), we constructed the kinetic model shown in Fig. 9, which we used for global fitting kinetic analysis (Fig. 10). The results of this analysis (Fig. 10, *A* and *B*) were in good agreement with those resulting from experimental fits (Fig. 9). In the proposed model RSK1 displays conformational heterogeneity, termed autoinhibited and released state, indicating the position of αL helix. The interaction of the released species with S100B is followed by an isomerization step. Note that S100B binding by the predominant autoinhibited species is not favorable. S100B binding therefore can be described as a combination of conformational selection and induced fit model (Fig. 10*B*). First, S100B can only bind to the free C-terminal tail. After the formation of the fuzzy complex, the anchored S100B can mediate further interactions with the kinase domain. The population of this "S100B-inhibited" state is ~44%, and it can share structural relationship with our crystal structure C. We speculate that this latter complex is responsible for the inactivation of the activated CTKD domain of RSK1.

To validate the apparent conformational heterogeneity of RSK1, we attempted to analyze the RSK1$_{CTKD}$ construct by

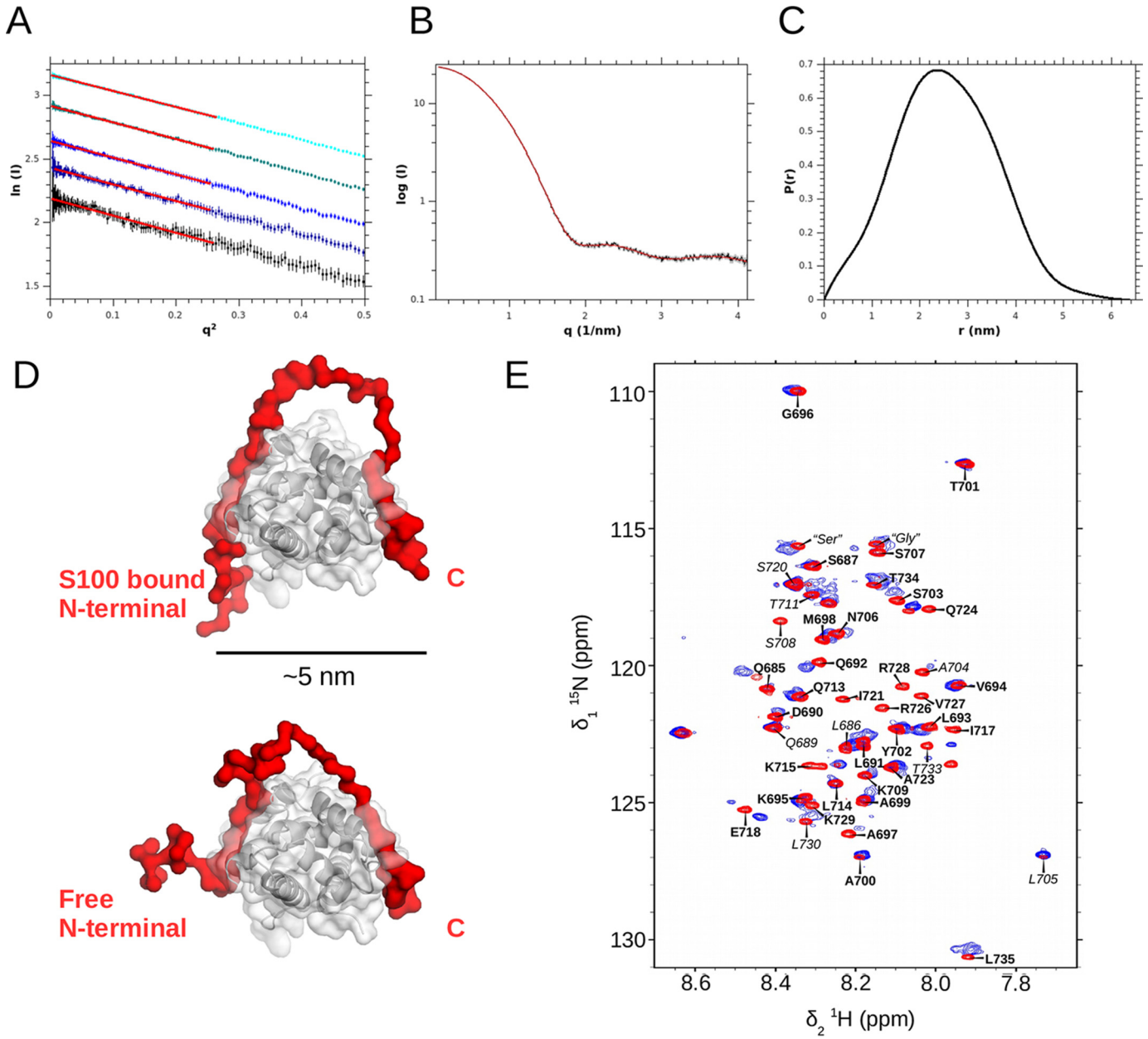

FIGURE 7. **Detailed analysis of the solution structure of the fuzzy S100B-RSK1 complex.** *A,* Guinier fit (*red lines*) to the obtained scattering curve in the concentration series. The measured concentrations of the isolated complex were 8.3, 3.8, 2.0, 0.8, and 0.5 mg/ml (from *cyan* to *black*). The curves were scaled and translated for clarity. Each measurement was averaged from 10 independently recorded frames. The scattering of the buffer was determined by measuring 10 frames before and after the sample measurements. *Error bars* show standard deviation from the mean. The calculated R_g was concentration independently 1.94 nm. *B,* experimental curve (*black line*) superimposed with the reconstructed scattering from distance distribution function (*red line*). *Error bars* are showed with *gray lines*. *C,* distance distribution function (so-called *P*(*r*) function) of the S100B-RSK1(683–735) complex derived from the experimental curve. The maximal dimension was determined to be 6.5 nm, and the calculated R_g was identical with the R_g from the Guinier fit (1.94 nm). *D,* two groups of independently simulated structures were identified by clustering. Representatives of the clusters are shown. The main differences among the clusters are the N-terminal conformations, which are either free or S100-bound. Note that this heterogeneous (10–15 residue long) N-terminal region is responsible for a large affinity increase in peptide truncation experiments. The average diameter of the simulated complexes is around 5 nm. The small tail in the *P*(*r*) function up to 6.5 nm can be an effect of the fuzziness of the intermediate and flanking part of the RSK1 peptide. *E,* overlay of the HSQC spectra of the free (*red*) and S100B complexed (*blue*) ^{15}N-labeled RSK1(683–735) peptide. Partial assignment of the free peptide is shown. The cloning "GS" artifacts are highlighted as "*Gly*" and "*Ser*." (*Bold* residues were assigned with larger confidence and low confidence is marked with *italic* characters.) Note that a fraction of peaks completely disappeared upon complex formation (*e.g.* Arg-726, Val-727, and Arg-728), whereas a fraction of peaks shows significant changes (*e.g.* Gln-692, Ser-703, or Leu-735). The remaining peaks do not show large changes upon S100B binding (*e.g.* Ser-687, Leu-714, or Ser-720).

SAXS (Fig. 10*C*). Unfortunately, all attempts to measure scattering of the S100B-RSK1$_{CTKD}$ complex failed, because the complex dissociated under gel filtration. Moreover, obtaining good SAXS data on the RSK1$_{CTKD}$ construct alone turned out to be technically challenging due to the protein's aggregation tendency. Fortunately, on-line gel filtration of the S100B-RSK1$_{CTKD}$ complex without Ca^{2+} finally gave useful scattering data on the RSK1$_{CTKD}$ construct. The measured pattern showed an acceptable fit with an RSK1 model obtained from the ERK2-RSK1$_{CTKD}$ heterodimeric crystal structure (χ = 1.00) (Fig. 10*C*) (13). In contrast, a more reasonable model (χ = 0.88) could be described as an ensemble of both "autoinhibited" and

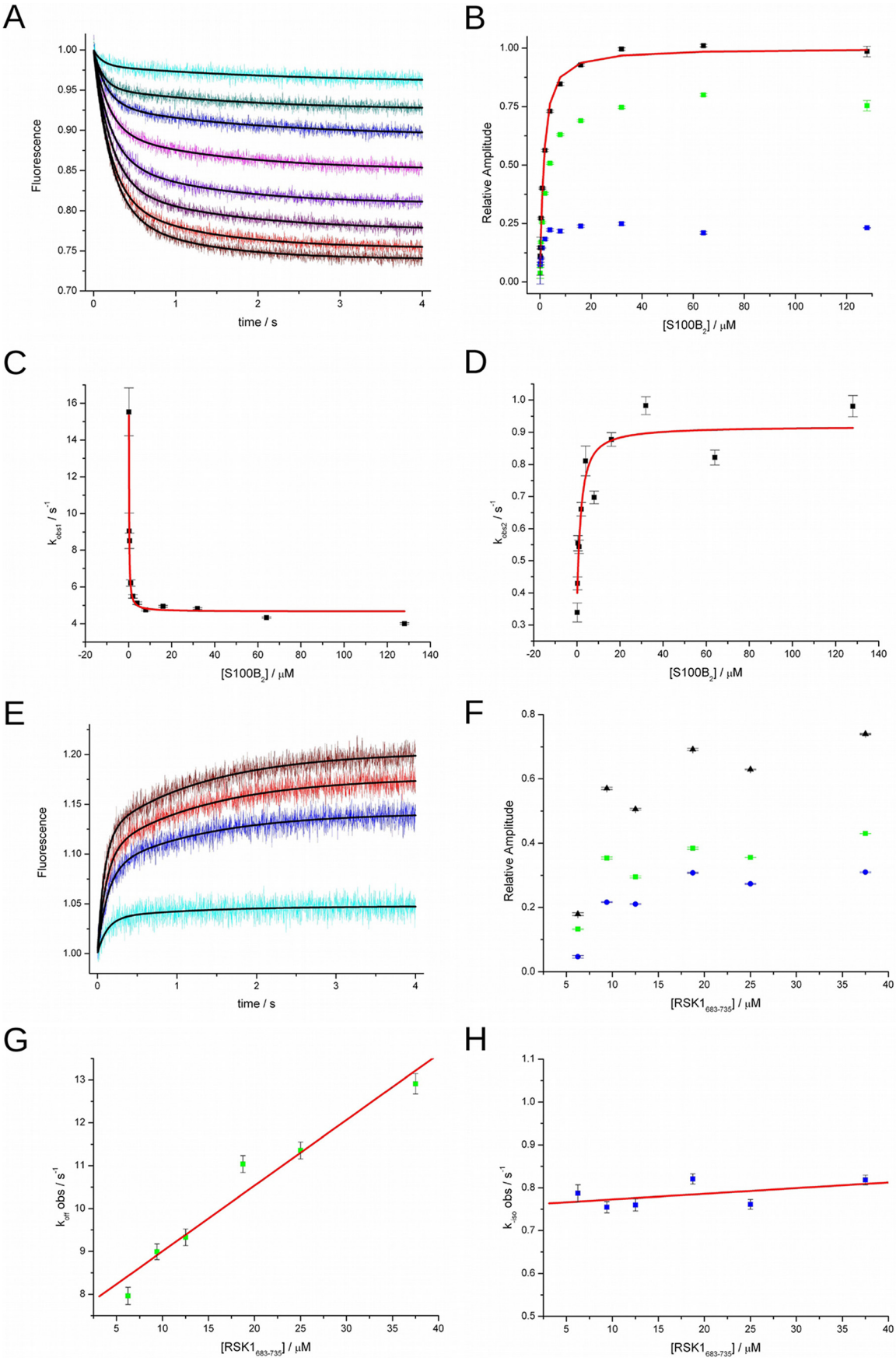
A
Fluorescence
time / s
B
Relative Amplitude
[S100B2] / μM
C
kobs1 / s-1
[S100B2] / μM
D
kobs2 / s-1
[S100B2] / μM
E
Fluorescence
time / s
F
Relative Amplitude
[RSK1683-735] / μM
G
koff obs / s-1
[RSK1683-735] / μM
H
kiso obs / s-1
[RSK1683-735] / μM

Global fit		Exponential analysis	
K_d,eq (μM)	~1	K_d,eq (A_{tot}, Binding) (μM)	1.3±0.1
k_C (s^{-1})	5.75±0.25	k_1 limit (Binding) (s^{-1})	4.8±0.2
k_I (s^{-1})	890±51		
k_{on} ($\mu M^{-1}s^{-1}$)	676±39		
k_{off} (s^{-1})	6.9±0.75	k_1 intercept (Dissociation) (s^{-1})	8.0±0.4
k_{iso} (s^{-1})	0.48±0.097	k_2 limit (Binding) (s^{-1}) (k_{iso} + k_{-iso})	0.96±0.06
k_{-iso} (s^{-1})	0.86±0.11	k_2 intercept (Dissociation) (s^{-1})	0.78±0.01
fluo RSK$_I$	1		
fluo RSK$_C$	1		
fluo [RSK-S100B]	0.79±0.01	A_1 max (rel. to initial value) (Binding)	0.8
fluo [RSK-S100B]*	0.64±0.02	A_2 max (rel. to initial value) (Binding)	0.75

FIGURE 9. **Comparison of the kinetic parameters based on the exponential analysis and the global fit.** The proposed model consists of two consecutive steps involving conformational selection or induced fit based steps. Free RSK1 is in a mixture of S100B binding competent and incompetent states (*1st step*). After complex formation (*2nd step*), the primary RSK1-S100B complex undergoes an additional isomerization step (*3rd step*; see also model in Fig. 10*B*). The kinetic constants were named based on the upper equation for the global fitting and according to Fig. 8 for the exponential analysis. Accurate assignation of k_i and k_{on} was not possible with our experimental setup. The listed parameters are the calculated lower limits for these parameters. However, these two variables show definite covariance, and simultaneous changes in their values do not influences the global, observed $K_{d,eq}$. Increasing the speed of these parameters results in a lowered fraction of the released state and therefore results in a more dominant conformational selection model.

"released" states of the CTKD (Fig. 10*D*). Although this may not be regarded as unambiguous validation of all the structural models proposed, it lends support to some aspects of the complex kinetic model.

Discussion

CaMK domains share similar architecture and therefore similar regulation. Their C-terminal extensions usually have an inhibitory effect on the kinase domain, and this autoinhibition needs to be released before the kinase can become enzymatically active. In many cases, this is achieved through CaM binding. In MAPKAPK-type kinases, the activation loop needs to be phosphorylated by a MAPK. Then the phosphorylated activation loop and the autoinhibitory element must go through substantial remolding at the active site (33). Hartman *et al.* (7) have recently reported that S100B can bind to RSK1 and suggested that this interaction is positioned to the same RSK1 C-terminal region where ERK2 also binds (12). However, the possibility that S100B may bind to the autoinhibitory RSK1 C-terminal region has not been postulated before. Based on our results, we conclude that CaM and S100B binding is structurally similar. However, their binding to cognate CaMK domains can have dramatically different functional readouts. CaM binding promotes CaMKII activity by stabilizing an open and active conformation of the kinase (see Fig. 1*A*), whereas S100B binding inhibits RSK1 activity, possibly by stabilizing a closed and autoinhibited form of RSK1, in addition to also directly blocking ERK2 recruitment. In the work of Hartman *et al.* (7), it was stated that S100B binding had no effect on the phosphorylation of the RSK hydrophobic motif. In the light of our *in vitro* kinase assay data and considering that MAPKAPK HM phosphorylation may occur reportedly in *trans* as well (34), this discrepancy may be explained by the insensitivity and/or nonspecific nature of the used antibody in the former report.

X-ray crystallographic, SAXS, and NMR-based structural analysis indicate that S100B forms a fuzzy complex with the C-terminal tail of RSK1. Disordered binding regions (IDRs) of proteins usually show flexibility only in their unbound state, but

FIGURE 8. **Tryptophan fluorescence-based kinetic experiments, exponential analysis.** *A,* binding traces of GST-RSK1$_{CTKD}$ and S100B fitted with a double exponential function. (The S100B concentration decreases from *red* to *blue*.) GST-RSK1$_{CTKD}$ Trp fluorescence transients were recorded upon rapidly mixing 1 μM RSK1$_{CTKD}$ with increasing concentrations of S100B$_2$ (0.125, 0.25, 0.5, 1, 2, 4, 8, 16, 32, 64, and 128 μM) in the stopped-flow instrument (post-mix concentrations are stated). *B,* amplitudes of the fitted exponentials of S100B-RSK1$_{CTKD}$ binding, expressed relative to the calculated maximal Trp fluorescence change. The amplitudes for the first exponential are colored in *green* and for the second exponential in *blue*. The total amplitudes (in *black*) were fit to a quadratic equation (K_d = 1.3 μM). *C,* observed rate constants of the first exponential phase. Note the decrease in the pseudo-first order region (>20 μM S100B). *D,* observed rate constants of the second exponential phase. *E,* dissociation of the S100B-RSK1$_{CTKD}$ complex monitored in kinetic chasing experiments. Trp fluorescence change was monitored upon rapidly mixing a premixture of GST-RSK1$_{CTKD}$ (1 μM) and S100B (15 μM) with increasing amounts of isolated RSK1 peptide (6.25, 9.38, 12.5, 18.75, 25, and 37.5 μM). (The chaser concentration decreases from *red* to *blue*.) Traces were fitted with a double exponential function. *F,* amplitudes of the fitted exponentials of the dissociation experiments, expressed relative to the calculated maximal Trp fluorescence change. Color scheme is identical to *B*. *G,* observed rate constants of the fast step (*green squares*) depend on the applied chaser peptide concentration. The increasing tendency of dissociation rate constants with chaser peptide concentration is indicative of active destabilization of the S100B-RSK1$_{CTKD}$ complex by the peptide. The actual off-rate constants were determined using linear extrapolation (*y* intercept). *H,* rate constant of the slower step (*blue squares*) is independent of chaser peptide concentration. See Fig. 9 for comparison of parameters determined by global fitting (Fig. 10) and exponential analysis (this figure). The measurement is representative of at least three sets of independent experiments, and *error bars* represent the standard deviations of the fitting.

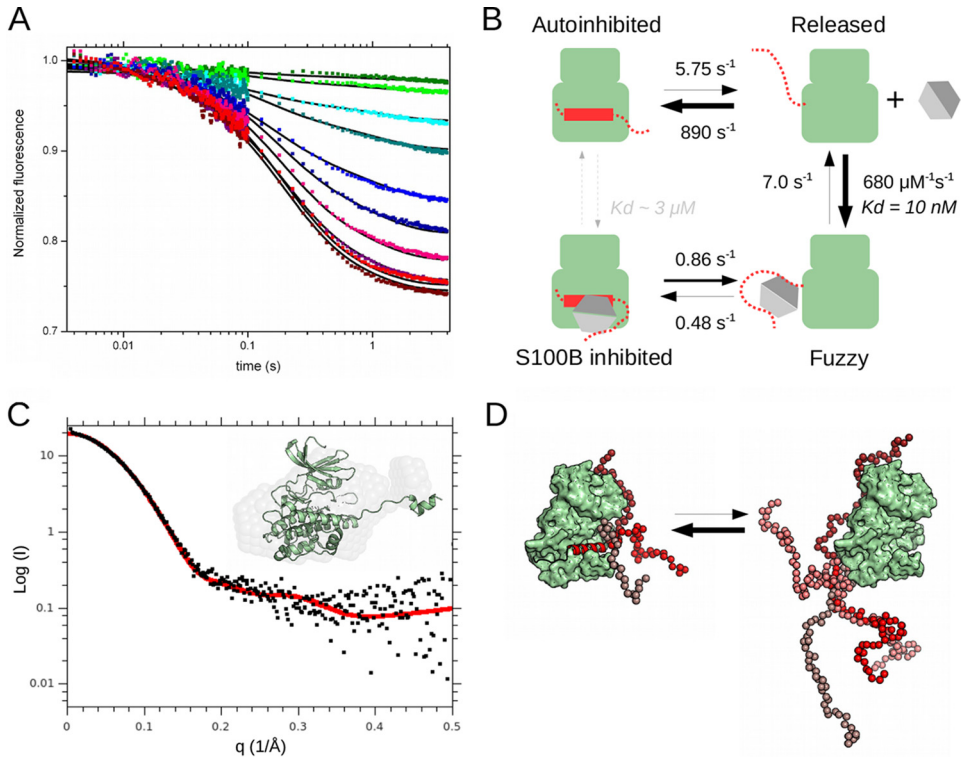

FIGURE 10. **Assembly of the S100B-RSK1 complex.** *A,* stopped-flow based kinetic analysis (presented in Fig. 8) by global fitting based on the model shown in *B* (*black lines*) (see also Fig. 9). (The S100B concentration decreases from *red* to *green*.) *B,* proposed kinetic model for RSK1-S100B interaction with the determined rate constants. In the unbound state, the kinase populates two forms: autoinhibited (>99%) and released (<1%). Regarding S100B binding, it is the released form that is capable of binding to S100B; therefore, this is an example for conformational selection. We hypothesized that the flexible C-terminal tail is the major source of the apparent conformational heterogeneity of RSK1, because this binding step has a $K_d = 10$ nM (6.97 s^{-1}/676 μM^{-1} s^{-1}). This value roughly corresponds to the strong steady-state binding affinity of an isolated peptide comprising this flexible C-terminal RSK1 tail (as the K_d of the S100B-RSK1(683–735) complex was determined to be 40 nM). The S100B-bound complex shows an additional isomerization step, as an example of induced fit, from the "fuzzy" complex into an "S100B-inhibited" state. An additional but kinetically blocked route is shown in *gray*. The theoretical K_d for this reaction is 2.85 μM. *C,* small angle x-ray scattering of $RSK1_{CTKD}$. The fit of the computed scattering curve based on the autoinhibitory state obtained from the ERK2-RSK1 crystal structure (13) is highlighted in *red* ($\chi = 1.00$). In the *inset* the crystal structure is displayed as superimposed to the averaged *ab initio* molecular envelope calculated by DAMMIN (27). *D,* most reasonable fit from EOM refinement (28) consisted of an ensemble of structures with mixed autoinhibitory and released states ($\chi = 0.88$).

upon partner binding they fold (35). In contrast, fuzzy complexes retain a degree of flexibility even in their bound form (19). They could be prevalent in interactomes, but they currently stay mostly uncharacterized due to limitations of our experimental approaches. Capturing static interactions from a fuzzy complex is challenging, and determining the in-solution structural ensemble is almost impossible. We managed to crystallize the minimal S100B-RSK1 complex in three different binding modes regarding the structure of the RSK1 C-terminal region. This was necessary to obtain a reliable structural ensemble by SAXS as experimentally determined crystallographic structural states could be used to model in-solution scattering. Interestingly, it was the fuzziest crystallographic model with only two small anchoring contacts between the flexible RSK1 C-terminal region and the dimeric S100B protein that matched the determined in-solution molecular ensemble the best. In this complex, a large part of the bound peptide is not involved in making contacts and is highly unstructured, which we also proved by solution NMR measurements. The fuzziness of the complex and the observed increase in helical content upon binding raise the question as to where and how a helix may form, albeit likely only transiently. Our diverse crystallographic models suggest that the shallow binding interface of S100B is able to interact with helical partners. Also, the distance between the two observed anchored regions is ~26 Å, which is connected by a 25-residue-long flexible linker. It is possible that the propensity for helix formation within this intervening region is highly increased because the motion of this relatively large linker is sterically limited by a clamping mechanism. It is noteworthy that a similar shallow groove of S100A4 mediates interaction with a helical peptide segment of NMIIA (3, 4).

The described mode of S100B binding directly to RSK1 is possible only if the inhibitory αL helix is released from the core kinase domain. If this is not the case, then S100B needs to pull out the helix from the active site. The first case would be a classical conformational selection mechanism, and the second one is an induced fit scenario. In theory, they can both be present, but our measured kinetic data suggest that the primary binding of S100B to $RSK1_{CTKD}$ can only be described with the conformational selection model. However, we also observed an induced fit step where the bound S100B further interacts with the kinase domain. This latter interaction could explain that S100B allosterically inhibits the activity of phosphorylated RSK1. Based on one of the crystallographic models (crystal structure C), it is likely that S100B can interact with the inhibitory αL helix *in situ*, and thus it may increase its stability in the autoinhibited *versus* the released state of RSK1 CTKD. Nevertheless, this complex is rather unlikely to form because the αG

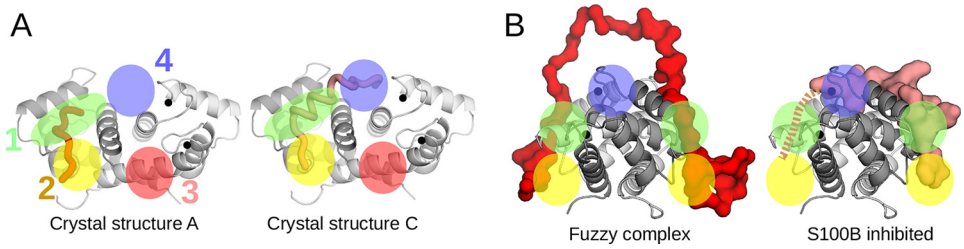

FIGURE 11. **Protein interaction surfaces of S100B and their relevance on differential S100B-RSK1 complex formation.** *A,* schematic view of RSK1-binding sites on S100B as projected on crystal structure A and C. Sites 1–3 had been previously identified as canonical S100B partner protein surfaces (39). However, site 3 is unoccupied in all S100B-RSK1 structures, whereas the novel site 4 is occupied in crystal structure C; therefore, site 4 may be uniquely used in the "S100B-inhibited" complex of RSK1. *B,* side view of the fuzzy and the S100B inhibited complex. In the fuzzy complex, site 4 remains free. Targeting this binding interface with small molecule inhibitors may tentatively interfere with only the S100B-inhibited complex but leaves fuzzy complex formation intact.

helix is in steric clash in the superimposed models. Releasing the αL inhibitory helix can cause a high degree of structural rearrangement, which can be ideal for the S100B bound inhibitory complex. From a kinetic perspective, the proposed mechanistic model can also be considered as a thermodynamic box (Fig. 10*B*). S100B binding to the autoinhibited state of the kinase can then directly result in the S100B inhibited complex, with a theoretically calculated K_d of <3 μM, which cannot be neglected compared with the observed binding constants. However, it is clear that that this path is kinetically blocked. Could the rearrangement of the αG helix be the reason for this kinetic block? Tentatively, the answer is yes; however, to describe this presumed S100B-RSK1 inhibitory complex in more detail, an atomic resolution structure of S100B in complex with the RSK1 CTKD is needed.

In malignant melanoma, the MAPK/ERK pathway is usually up-regulated by activating mutations of upstream kinases. This could result in hyperphosphorylation and hyperactivation of RSK1. However, overexpression of S100B in melanoma protects RSK1 against active ERK2 and in turn from autophosphorylation. The mechanistic explanation why S100B inhibition of RSK1 activation is a hallmark feature in melanoma is not understood. Hartman *et al.* (7) also showed that the subcellular localization of RSK1 is altered by S100B, which could shift remaining RSK1 activity into the cytoplasm. These effects may be beneficial to melanoma cells by negatively affecting important tumor suppressor proteins such as DAPK1, LKB1, or TSC2 (10, 36, 37). Although little is known about the precise mechanism behind RSK1 localization, cellular studies showed that activation of the NTKD involving both AL and HM phosphorylation is essential to nuclear accumulation (38). CTKD inhibition by S100B can directly affect HM phosphorylation and therefore the NTKD AL phosphorylation, too.

Before this study, three binding pockets were identified on S100B (Fig. 11*A*) (39). Selective targeting of these sites is already a promising opportunity for the treatment of malignant melanoma (9). Here, we showed that the fuzzy complex uses site 1 and site 2 simultaneously, whereas the inhibitory complex involves an asymmetric fourth binding site, which is placed between the classical symmetric binding pockets (Fig. 11). Targeting the classical binding sites can inhibit interactions of S100B indiscriminately, but targeting of this middle binding pocket may be a highly selective inhibitor for the assembly of the S100B-RSK1 inhibitory complex. Based on the observation that primary complex formation only yields the fuzzy complex where this fourth binding site remains free, this novel site may be a potent switch that can freeze the S100B-RSK1$_{CTKD}$ complex into a CaMK-CaM type complex. Stabilization of this latter conformation would presumably promote activation of the kinase, thus turning S100B into an activator of the ERK pathway rather than an inhibitor. Overall, our data and structural models potentially may open up avenues for selective modulation, inhibition and activation alike, of RSK1 activity. In turn, this could enable mapping out the physiological consequences of the apparent signaling cross-talk between a Ca^{2+}-dependent protein and an important kinase regulator of cell growth.

Author Contributions—G. G. and A. A. designed and performed the experiments and analyzed the data. B. K., G. K., and M. K. contributed in designing the experiments and analyzing data. G. G., A. R., and L. N. oversaw the research and wrote the paper. All authors reviewed the results and approved the final version of the manuscript.

Acknowledgments—We thank the staff members at beamlines PXIII of Swiss Light Source (SLS) and ID23, ID30, and BM29 of European Synchrotron Radiation Facility (ESRF) for assistance in data collection.

References

1. Donato, R. (2001) S100: a multigenic family of calcium-modulated proteins of the EF-hand type with intracellular and extracellular functional roles. *Int. J. Biochem. Cell Biol.* **33,** 637–668
2. Marenholz, I., Heizmann, C. W., and Fritz, G. (2004) S100 proteins in mouse and man: from evolution to function and pathology (including an update of the nomenclature). *Biochem. Biophys. Res. Commun.* **322,** 1111–1122
3. Kiss, B., Duelli, A., Radnai, L., Kékesi, K. A., Katona, G., and Nyitray, L. (2012) Crystal structure of the S100A4-nonmuscle myosin IIA tail fragment complex reveals an asymmetric target binding mechanism. *Proc. Natl. Acad. Sci. U.S.A.* **109,** 6048–6053
4. Elliott, P. R., Irvine, A. F., Jung, H. S., Tozawa, K., Pastok, M. W., Picone, R., Badyal, S. K., Basran, J., Rudland, P. S., Barraclough, R., Lian, L. Y., Bagshaw, C. R., Kriajevska, M., and Barsukov, I. L. (2012) Asymmetric mode of Ca^{2+}-S100A4 interaction with nonmuscle myosin IIA generates nanomolar affinity required for filament remodeling. *Structure.* **20,** 654–666
5. Bresnick, A. R., Weber, D. J., and Zimmer, D. B. (2015) S100 proteins in cancer. *Nat. Rev. Cancer.* **15,** 96–109
6. Riuzzi, F., Sorci, G., and Donato, R. (2006) S100B Stimulated myoblast proliferation and inhibits myoblast differentiation by independently stimulating ERK1/2 and inhibiting p38 MAPK. *J. Cell. Physiol.* **207,** 461–470
7. Hartman, K. G., Vitolo, M. I., Pierce, A. D., Fox, J. M., Shapiro, P., Martin,

S. S., Wilder, P. T., and Weber, D. J. (2014) Complex formation between s100b protein and the p90 ribosomal S6 kinase (RSK) in malignant melanoma is calcium-dependent and inhibits extracellular signal-regulated kinase (ERK)-mediated phosphorylation of RSK. *J. Biol. Chem.* **289,** 12886–12895
8. Gogas, H., Eggermont, A. M., Hauschild, A., Hersey, P., Mohr, P., Schadendorf, D., Spatz, A., and Dummer, R. (2009) Biomarkers in melanoma. *Ann. Oncol.* **20,** vi8–vi13
9. Hartman, K. G., McKnight, L. E., Liriano, M. A., and Weber, D. J. (2013) The evolution of S100B inhibitors for the treatment of malignant melanoma. *Future Med. Chem.* **5,** 97–109
10. Romeo, Y., Zhang, X., and Roux, P. P. (2012) Regulation and function of the RSK family of protein kinases. *Biochem. J.* **441,** 553–569
11. Cargnello, M., and Roux, P. P. (2011) Activation and function of the MAPKs and their substrates, the MAPK-activated protein kinases. *Microbiol. Mol. Biol. Rev.* **75,** 50–83
12. Garai, Á., Zeke, A., Gógl, G., Törő, I., Fördős, F., Blankenburg, H., Bárkai, T., Varga, J., Alexa, A., Emig, D., Albrecht, M., and Reményi, A. (2012) Specificity of linear motifs that bind to a common mitogen-activated protein kinase docking groove. *Sci. Signal.* **5,** ra74
13. Alexa, A., Gógl, G., Glatz, G., Garai, Á., Zeke, A., Varga, J., Dudás, E., Jeszenői, N., Bodor, A., Hetényi, C., and Reményi, A. (2015) Structural assembly of the signaling competent ERK2–RSK1 heterodimeric protein kinase complex. *Proc. Natl. Acad. Sci.* **112,** 2711–2716
14. Malakhova, M., Tereshko, V., Lee, S.-Y., Yao, K., Cho, Y.-Y., Bode, A., and Dong, Z. (2008) Structural basis for activation of the autoinhibitory C-terminal kinase domain of p90 RSK2. *Nat. Struct. Mol. Biol.* **15,** 112–113
15. Rellos, P., Pike, A. C., Niesen, F. H., Salah, E., Lee, W. H., von Delft, F., and Knapp, S. (2010) Structure of the CaMKIIδ/calmodulin complex reveals the molecular mechanism of CaMKII kinase activation. *PLoS Biol.* **8,** e1000426
16. Pearce, L. R., Komander, D., and Alessi, D. R. (2010) The nuts and bolts of AGC protein kinases. *Nat. Rev. Mol. Cell Biol.* **11,** 9–22
17. Frödin, M., Antal, T. L., Dümmler, B. A., Jensen, C. J., Deak, M., Gammeltoft, S., and Biondi, R. M. (2002) A phosphoserine/threonine-binding pocket in AGC kinases and PDK1 mediates activation by hydrophobic motif phosphorylation. *EMBO J.* **21,** 5396–5407
18. Chrestensen, C. A, and Sturgill, T. W. (2002) Characterization of the p90 ribosomal S6 kinase 2 carboxyl-terminal domain as a protein kinase. *J. Biol. Chem.* **277,** 27733–27741
19. Tompa, P., and Fuxreiter, M. (2008) Fuzzy complexes: polymorphism and structural disorder in protein-protein interactions. *Trends Biochem. Sci.* **33,** 2–8
20. Weichenberger, C. X., and Rupp, B. (2014) Ten years of probabilistic estimates of biocrystal solvent content: New insights via nonparametric kernel density estimate. *Acta Crystallogr. D Biol. Crystallogr.* **70,** 1579–1588
21. Kabsch, W. (2010) XDS. *Acta Crystallogr. D Biol. Crystallogr.* **66,** 125–132
22. McCoy, A. J., Grosse-Kunstleve, R. W., Adams, P. D., Winn, M. D., Storoni, L. C., and Read, R. J. (2007) Phaser crystallographic software. *J. Appl. Crystallogr.* **40,** 658–674
23. Ostendorp, T., Diez, J., Heizmann, C. W., and Fritz, G. (2011) The crystal structures of human S100B in the zinc- and calcium-loaded state at three pH values reveal zinc ligand swapping. *Biochim. Biophys. Acta* **1813,** 1083–1091
24. Adams, P. D., Afonine, P. V., Bunkóczi, G., Chen, V. B., Davis, I. W., Echols, N., Headd, J. J., Hung, L.-W., Kapral, G. J., Grosse-Kunstleve, R. W., McCoy, A. J., Moriarty, N. W., Oeffner, R., Read, R. J., Richardson, D. C., *et al.* (2010) PHENIX: a comprehensive Python-based system for macromolecular structure solution. *Acta Crystallogr. D Biol. Crystallogr.* **66,** 213–221
25. Emsley, P., Lohkamp, B., Scott, W. G., and Cowtan, K. (2010) Features and development of Coot. *Acta Crystallogr. D Biol. Crystallogr.* **66,** 486–501
26. Micsonai, A., Wien, F., Kernya, L., Lee, Y.-H., Goto, Y., Réfrégiers, M., and Kardos, J. (2015) Accurate secondary structure prediction and fold recognition for circular dichroism spectroscopy. *Proc. Natl. Acad. Sci. U.S.A.* **112,** E3095–E3103
27. Petoukhov, M. V., Franke, D., Shkumatov, A. V., Tria, G., Kikhney, A. G., Gajda, M., Gorba, C., Mertens, H. D., Konarev, P. V., and Svergun, D. I. (2012) New developments in the ATSAS program package for small-angle scattering data analysis. *J. Appl. Crystallogr.* **45,** 342–350
28. Tria, G., Mertens, H. D., Kachala, M., and Svergun, D. I. (2015) Advanced ensemble modelling of flexible macromolecules using x-ray solution scattering. *IUCrJ.* **2,** 207–217
29. Keller, R. (2004) *The Computer Aided Resonance Assignment Tutorial,* Cantina Verlag, Switzerland
30. Gaertner, T. R., Kolodziej, S. J., Wang, D., Kobayashi, R., Koomen, J. M., Stoops, J. K., and Waxham, M. N. (2004) Comparative analyses of the three-dimensional structures and enzymatic properties of α, β, γ, and δ isoforms of Ca^{2+}-calmodulin-dependent protein kinase II. *J. Biol. Chem.* **279,** 12484–12494
31. Gavin, A. C., and Nebreda, A. R. (1999) A MAP kinase docking site is required for phosphorylation and activation of p90(rsk)/MAPKAP kinase-1. *Curr. Biol.* **9,** 281–284
32. Li, D., Fu, T.-M., Nan, J., Liu, C., Li, L.-F., and Su, X.-D. (2012) Structural basis for the autoinhibition of the C-terminal kinase domain of human RSK1. *Acta Crystallogr. D Biol. Crystallogr.* **68,** 680–685
33. Underwood, K. W., Parris, K. D., Federico, E., Mosyak, L., Czerwinski, R. M., Shane, T., Taylor, M., Svenson, K., Liu, Y., Hsiao, C. L., Wolfrom, S., Maguire, M., Malakian, K., Telliez, J. B., Lin, L. L., *et al.* (2003) Catalytically active MAP KAP kinase 2 structures in complex with Staurosporine and ADP reveal differences with the autoinhibited enzyme. *Structure* **11,** 627–636
34. Zaru, R., Ronkina, N., Gaestel, M., Arthur, J. S., and Watts, C. (2007) The MAPK-activated kinase Rsk controls an acute Toll-like receptor signaling response in dendritic cells and is activated through two distinct pathways. *Nat. Immunol.* **8,** 1227–1235
35. Dunker, A. K., Lawson, J. D., Brown, C. J., Williams, R. M., Romero, P., Oh, J. S., Oldfield, C. J., Campen, A. M., Ratliff, C. M., Hipps, K. W., Ausio, J., Nissen, M. S., Reeves, R., Kang, C., Kissinger, C. R., *et al.* (2001) Intrinsically disordered protein. *J. Mol. Graph. Model.* **19,** 26–59
36. Anjum, R., Roux, P. P., Ballif, B. A., Gygi, S. P., and Blenis, J. (2005) The tumor suppressor DAP kinase is a target of RSK-mediated survival signaling. *Curr. Biol.* **15,** 1762–1767
37. Romeo, Y., Moreau, J., Zindy, P.-J., Saba-El-Leil, M., Lavoie, G., Dandachi, F., Baptissart, M., Borden, K. L. B., Meloche, S., and Roux, P. P. (2013) RSK regulates activated BRAF signalling to mTORC1 and promotes melanoma growth. *Oncogene* **32,** 2917–2926
38. Gao, X., Chaturvedi, D., and Patel, T. B. (2012) Localization and retention of p90 ribosomal S6 kinase 1 in the nucleus: implications for its function. *Mol. Biol. Cell.* **23,** 503–515
39. Cavalier, M. C., Pierce, A. D., Wilder, P. T., Alasady, M. J., Hartman, K. G., Neau, D. B., Foley, T. L., Jadhav, A., Maloney, D. J., Simeonov, A., Toth, E. A., and Weber, D. J. (2014) Covalent small molecule inhibitors of Ca^{2+}-bound S100B. *Biochemistry* **53,** 6628–6640
40. Ikuta, M., Kornienko, M., Byrne, N., Reid, J. C., Mizuarai, S., Kotani, H., and Munshi, S. K. (2007) Crystal structures of the N-terminal kinase domain of human RSK1 bound to three different ligands: Implications for the design of RSK1 specific inhibitors. *Protein Sci.* **16,** 2626–2635
41. van Dieck, J., Teufel, D. P., Jaulent, A. M., Fernandez-Fernandez, M. R., Rutherford, T. J., Wyslouch-Cieszynska, A., and Fersht, A. R. (2009) Post-translational modifications affect the interaction of S100 proteins with tumor suppressor p53. *J. Mol. Biol.* **394,** 922–930